Chaotic dynamics of flexible Euler-Bernoulli beams

J. Awrejcewicz,[1,a)] A. V. Krysko,[2,b)] I. E. Kutepov,[3,c)] N. A. Zagniboroda,[3,d)] V. Dobriyan,[3,e)] and V. A. Krysko[3,f)]
[1]*Department of Automation, Biomechanics and Mechatronics, Lodz University of Technology, 1/15 Stefanowski St., 90-924 Lodz, Poland and Department of Vehicles, Warsaw University of Technology, 84 Narbutta St., 02-524 Warsaw, Poland*
[2]*Department of Applied Mathematics and Systems Analysis, Saratov State Technical University, Politehnicheskaya 77, 410054 Saratov, Russian Federation*
[3]*Department of Mathematics and Modeling, Saratov State Technical University, Politehnicheskaya 77, 410054 Saratov, Russian Federation*

(Received 13 May 2013; accepted 4 November 2013; published online 9 December 2013)

Mathematical modeling and analysis of spatio-temporal chaotic dynamics of flexible simple and curved Euler-Bernoulli beams are carried out. The Kármán-type geometric non-linearity is considered. Algorithms reducing partial differential equations which govern the dynamics of studied objects and associated boundary value problems are reduced to the Cauchy problem through both Finite Difference Method with the approximation of $O(c^2)$ and Finite Element Method. The obtained Cauchy problem is solved via the fourth and sixth-order Runge-Kutta methods. Validity and reliability of the results are rigorously discussed. Analysis of the chaotic dynamics of flexible Euler-Bernoulli beams for a series of boundary conditions is carried out with the help of the qualitative theory of differential equations. We analyze time histories, phase and modal portraits, autocorrelation functions, the Poincaré and pseudo-Poincaré maps, signs of the first four Lyapunov exponents, as well as the compression factor of the phase volume of an attractor. A novel scenario of transition from periodicity to chaos is obtained, and a transition from chaos to hyper-chaos is illustrated. In particular, we study and explain the phenomenon of transition from symmetric to asymmetric vibrations. Vibration-type charts are given regarding two control parameters: amplitude q_0 and frequency ω_p of the uniformly distributed periodic excitation. Furthermore, we detected and illustrated how the so called temporal-space chaos is developed following the transition from regular to chaotic system dynamics.
[http://dx.doi.org/10.1063/1.4838955]

Several recent studies address the issue of turbulent behavior of structural members. In particular, a weak wave turbulence has been observed experimentally in thin elastic plates. We are aimed on considering the issue of a transition from regular to spatio-temporal dynamics of the Euler-Bernoulli beams. Contrary to majority of works reducing the infinite dimensional problem governed by PDEs to that of a few (mainly two) degrees of freedom, we propose and apply more rigorous and numerically validated reduction to a system of ODEs (ordinary differential equations) using both FDM (Finite Difference Method) and FEM (Finite Element Method). The obtained novel results include various transitions into chaotic and hyper-chaotic vibration regimes of the studied Euler-Bernoulli beams. We also illustrate and discuss their spatio-temporal chaotic dynamics. We show that the scenario of transition from regular dynamics into chaotic one is realized simultaneously in time and space. We also illustrate how the application of wavelet analysis allows us to detect and monitor novel non-linear phenomena exhibited by studied beams, which cannot be found using the standard FFT (Fast Fourier Transform) methods.

[a)]awrejcew@p.lodz.pl
[b)]anton.krysko@gmail.com
[c)]iekutepov@gmail.com
[d)]tssrat@mail.ru
[e)]Dobriy88@yandex.ru
[f)]tak@san.ru

I. INTRODUCTION

Non-linear vibrations of beams are studied by numerous researchers. Many problems occurring in real constructions of mechanical and civil engineering can be reduced to beam analysis. Many researchers take into consideration various types of beam materials, shape, design, and hence various types of non-linearity models are applied including geometric, physical and design non-linearity.

Wang[1] studied transverse vibrations of a tapered beam by Frobenius method and generalized hypergeometric functions while solving the Euler-Bernoulli equations with variable coefficients. The Adomian decomposition method was used by Hsu *et al.*[2] to solve the eigenvalue problem of the uniform Timoshenko beams. Yeih *et al.*[3] estimated natural frequencies and modes of the Euler-Bernoulli beams using the singular value decomposition. Pitchfork bifurcations, stability of equilibrium, and the post bifurcation velocity range of the Euler-Bernoulli beam with fixed ends were analyzed by Moon and Wickert.[4]

Abu-Hilal[5] obtained exact solutions in closed form of forced vibrations of prismatic damped Euler-Bernoulli beams applying Green's function.

Gutschmidt and Gottlieb[6] analyzed bifurcations and orbital stability loss of N non-linear coupled micro-electromechanical parametrically actuated Euler-Bernoulli beams.

On the other hand, the Euler-Bernoulli curved beams belong to less investigated, and hence we mention only a few works devoted to this problem. The exact formula between deflections and resultants of the Timoshenko and Euler-Bernoulli curved beams was proposed by Lim *et al.*[7] A complete second order deformations field together with the governing Euler-Bernoulli beams dynamic equations is reported in Ref. 8. Zohoor and Khorsandijou[9] developed a novel 3D Euler-Bernoulli beam model governed by ten coupled PDEs.

On the other hand, chaotic dynamics of beams is rather rarely investigated, since mainly the problems regarding a few degrees of freedom of lumped mechanical systems are addressed, i.e., strong truncation of the original infinite model is introduced. Here, we mention only a few fundamental works,[10–13] including also the research published by the co-authors of this paper.[14,15]

This paper also addresses another novel research track regarding *turbulence* and *wave turbulence* in a solid. In this context, structural members (plates and shells) displaying large amplitude motions reveal weak turbulent dynamics quantified via broad band Fourier components. This point of view has been initiated by a series of works devoted to numerical analysis,[16–25] and recently supported by experimental investigations reported by Nagai *et al.*[26] and Maruyama *et al.*[27] The von Kármán kinematic plate model was verified experimentally regarding its behavior.[28–34]

Another challenging part of this paper concerns the application of wavelet analysis to chaotic/turbulent dynamics of structural members which allows us to detect, contrary to the standard approach relying on the FFT (Fast Fourier Transform), new dynamic phenomena (see Refs. 35–39 for more details).

The analysis of available references implies that works addressing the problems of dynamics of the Euler-Bernoulli beams are restricted to the approximation through the systems with a few degrees of freedom. In addition, phenomena associated with the transition from regular to chaotic dynamics are sometimes not widely illustrated and discussed. There is a lack of rigorous analysis of the chaotic dynamics of structural members through a spectrum of the Lyapunov exponents and in many cases algorithms for the estimation of the Lyapunov spectrum are doubtful. There is a need to compute a scenario of transitions from regular to spatio-temporal chaotic dynamics of flexible Euler-Bernoulli beams. There is no report, either, on the construction of the so called vibration-type charts regarding non-linear dynamics of beams (periodicity, chaos, bifurcations) versus control parameters. Chaotic vibrations of the Euler-Bernoulli beams within a wide interval of the exciting load frequency are not analyzed. Our aim is to fulfill these gaps in the existing literature dedicated to the analysis of dynamics of the Euler-Bernoulli beams.

II. A SIMPLE EULER-BERNOULLI BEAM MODEL

Achievements in the field of numerical solutions to PDEs allowed us to use the non-linear theories of mechanics of deformable bodies and hence to solve directly numerous problems of vibrations of complex structural mechanical systems. Flexible beams are widely applied as members of the constructions of aviation and rocket-cosmic industries and they are frequently used by car manufacturers and factories producing various measurement devices. The investigation of such elements subjected to dynamic load action belongs to one of the fundamental steps in carrying out the full analysis of the whole construction. In particular, it is important to study the dynamic regime evolution versus external excitation parameters (amplitude and frequency) and dispersion properties of a surrounding medium.

Application of the deterministic chaos theory allowed us to discover new dynamic phenomena of nonlinear vibrations of beams, panels, plates and shells, and their interactions. In this work, we study one-layer thin flexible beams with length a and height h excited by normal load $q(x,t)$ (see Fig. 1).

The mathematical model relies on the following hypotheses: (1) deformations remain normal to the mean beam surface and hence the height of the beam cross section is unchanged; (2) although we do not take into account inertial effects of the rotation of beam elements, we consider inertial forces responsible for beam displacement along the normal; (3) external forces do not change their direction during beam deformations; and (4) geometric non-linearity is taken in the form proposed by Kármán.

The so far mentioned hypotheses are based on the Euler-Bernoulli ideas, and even though they are within the first modeling approximation, they are accurate enough and suitable for the numerical analysis.

Non-linear PDEs governing beam dynamics describe equations of motion of a beam element with the energy dissipation, and they have the following non-dimensional form:

$$\begin{aligned}
&\frac{\partial^2 u}{\partial x^2} + L_3(w,w) - \frac{\partial^2 u}{\partial t^2} = 0,\\
&\frac{1}{\lambda^2}\left\{-\frac{1}{12}\frac{\partial^4 w}{\partial x^4} + L_1(u,w) + L_2(w,w)\right\} + q - \frac{\partial^2 w}{\partial t^2} - \varepsilon\frac{\partial w}{\partial t} = 0;\\
&L_1(u,w) = \frac{\partial^2 u}{\partial x^2}\frac{\partial w}{\partial x} + \frac{\partial u}{\partial x}\frac{\partial^2 w}{\partial x^2};\\
&L_2(w,w) = \frac{3}{2}\left(\frac{\partial w}{\partial x}\right)^2\frac{\partial^2 w}{\partial x^2};\quad L_3(w,w) = \frac{\partial w}{\partial x}\frac{\partial^2 w}{\partial x^2},
\end{aligned} \tag{1}$$

where $L_1(u,w)$, $L_2(w,w)$, and $L_3(w,w)$ are the non-linear operators; $w(x,t)$ represents beam deflection in the normal

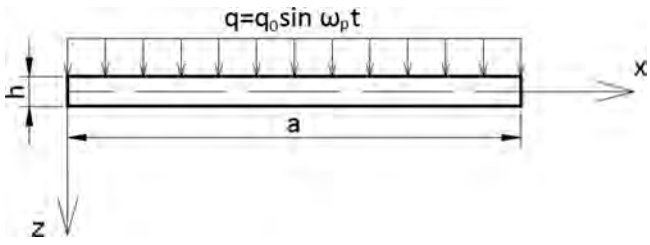

FIG. 1. A studied beam.

direction; $u(x,t)$, beam displacement in the beam longitudinal direction; ε, damping coefficient; E, Young modulus; h, beam height; γ, specific material gravity; g, acceleration due to gravity; t, time; and $q = q_0\sin(\omega_p t)$, external load.

The non-dimensional parameters are introduced in the following way:

$$\lambda = \frac{a}{h}; \quad \bar{w} = \frac{w}{h}; \quad \bar{u} = \frac{ua}{h^2}; \quad \bar{x} = \frac{x}{a}; \quad \bar{t} = \frac{t}{\tau};$$
$$\tau = \frac{a}{p}; \quad p = \sqrt{\frac{Eg}{\gamma}}; \quad \bar{\varepsilon} = \frac{a}{p}; \quad \bar{q} = \frac{qa^4}{h^4 E}. \tag{2}$$

Bars in Eqs. (1) are omitted. Equations (1) are supplemented by one of the following boundary conditions:

1. Fixed support (both ends are fixed) ($x = 0$, $x = a$)

$$w(0,t) = w(a,t) = u(0,t) = u(a,t) = w'_x(0,t) = w'_x(a,t) = 0. \tag{3}$$

2. Pinned (hinged) support (both ends are pinned) ($x = 0$, $x = a$)

$$w(0,t) = w(a,t) = u(0,t) = u(a,t) = w''_{xx}(0,t) = w''_{xx}(a,t) = 0. \tag{4}$$

3. One beam end is fixed ($x = 0$), whereas the second one is pinned ($x = a$)

$$w(0,t) = w(a,t) = u(0,t) = u(a,t) = w'_x(0,t) = w''_x(a,t) = 0. \tag{5}$$

4. One beam end is fixed ($x = 0$), whereas the second one is free ($x = a$)

$$w(0,t) = w'_x(0,t) = u(0,t) = 0;\ M_x(a,t) = N_x(a,t) = Q_x(a,t) = 0 \tag{6}$$

and the following initial conditions:

$$w(x,0) = \dot{w}(x,0) = u(x,0) = \dot{u}(x,0). \tag{7}$$

III. METHODS OF SOLUTION

We cannot solve analytically Eqs. (1)–(7), and hence we solve them numerically by reduction to ODEs using Finite Difference Method (FDM) of the second order with respect to x, and using Finite Element Method (FEM).

A. FDM application

In order to reduce PDEs to ODEs, we apply the finite difference approximations relying on the development into the Taylor series in the vicinity of point x_i. Consider the mesh

$$G_N = \{0 \le x_i \le 1, x_i = i/N, i = 0, ..., N\}.$$

We introduce the following difference operators with the approximation $O(c^2)$, where c stands for the spatial co-ordinate step:

$$\Lambda_x(\cdot_i) = \frac{(\cdot)_{i+1} - (\cdot)_{i-1}}{2c},$$
$$\Lambda_{x^2}(\cdot_i) = \frac{(\cdot)_{i+1} - 2(\cdot)_i + (\cdot)_{i-1}}{c^2},$$
$$\Lambda_{x^4}(\cdot_i) = \frac{(\cdot)_{i+2} - (\cdot)_{i+1} + 6(\cdot)_i - (\cdot)_{i-1} + (\cdot)_{i-2}}{c^4}.$$

We transit from PDEs (1) to the following ODEs with respect to time co-ordinate:

$$\ddot{u}_\tau = \Lambda_{x^2}(u_i) + \Lambda_x(w_i)\Lambda_{x^2}(w_i),$$
$$\ddot{w}_t + \varepsilon\dot{w}_t = \lambda^2\Big\{-\frac{1}{12}\Lambda_{x^4}(w_i) + \Lambda_{x^2}(u_i)\Lambda_x(w_i) + \Lambda_{x^2}(w_i)\Lambda_x(u_i) + \frac{3}{2}(\Lambda_x(w_i))^2\Lambda_{x^2}(w_i) + q\Big\}. \tag{8}$$

The system of the second order ODEs (8) with the associated boundary and initial conditions is then transformed to the first-order ODEs. The latter system is solved via the Runge-Kutta methods of the fourth and sixth orders.

B. FEM application

Now, we apply FEM to system (1)–(7). In general, FEM is applied either via minimization of various energy functionals or by other approximation methods like the Bubnov-Galerkin approach. In the latter approach functions, $w(x)$ and $u(x)$ are approximated by the following forms:

$$\widehat{w} = \sum_{i=1}^{N}\psi_i(x)w_i, \quad \widehat{u} = \sum_{i=1}^{N}\varphi_i(x)u_i, \tag{9}$$

where u_i and w_i denote the values of functions $u(x)$ and $w(x)$ in nodes $(i = 1, ..., N)$, respectively; $\varphi_i(x)$ and $\psi_i(x)$ are the known analytical test (mode) functions.

Owing to the theory of FEM, 4 degrees of freedom $(w_1, w_2, \theta_1, \theta_2)$ are attached to each beam element, and the following cubic polynomial is applied:

$$w(x) = a_1 + a_2x + a_3x^2 + a_4x^3,$$
$$\theta(x) = -\frac{dw}{dx} = -\left(a_2 + 2a_3x + 3a_4x^2\right). \tag{10}$$

After determination of the values of constants, the following formula for the approximation of $w(x)$ is proposed:

$$w = [N_w]\{W\}, \tag{11}$$

where $[N_w] = (1 - 3\xi^2 + 2\xi^3; -l\xi(\xi - 1)^2; 3\xi^2 - 2\xi^3; -l\xi(\xi^2 - \xi))$ is mode matrix; $\{W\} = (w_1,\ \theta_1,\ w_2,\ \theta_2)^T$, node displacements matrix; $\xi = x/a$, non-dimensional quantity (local co-ordinate). The approximation of displacement $u(x)$ is as follows:

$$u = [N_u]\{U\}, \tag{12}$$

where $[N_u] = (1 - \xi; \xi)$ $\{U\} = \left(u_1 \quad u_2\right)^T$. Applying the Bubnov-Galerkin procedure the following equations are obtained:

$$M_1\ddot{W}(t) + C_1\dot{W}(t) + K_1W(t) = F_1(q(t), U(t)),$$
$$M_2\ddot{U}(t) + C_2\dot{U}(t) + K_2U(t) = F_2(W(t)), \quad (13)$$

where M_i, C_i, K_i are the mass, damping and stiffness matrices, respectively.

C. Reliability of results

In order to verify the numerical results obtained via FDM, they were compared with the FEM solutions. Figure 2 includes the signals $(w(0.5,t))$, power spectra obtained through the FFT, as well as the 3D Morlet wavelet spectra.[17]

The obtained results correspond to the following fixed parameters: $\lambda = 50$, $n = 80$, $\varepsilon = 1$, $\omega_p = 8.625$, $q_0 = 5.5 \times 10^4$, where n denotes the number of partitions $x \in [0,1]$. In Figure 2, the following notation is used: A—$w(0.5;t)$, $t \in [1836-1838]$; B—Fourier power spectra yielded by FDM and FEM; C—Morlet wavelet spectra associated with FDM and FEM. The following relations hold for the frequencies: ω_1, ω_p- independent, $\omega_2 = 1/5\omega_1$, $\omega_3 = 3/5\omega_1$, $\omega_4 = 7/5\omega_1$, $\omega_5 = 9/5\omega_1$, $\omega_6 = 11/5\omega_1$, $\omega_7 = 7/8\omega_p$, $\omega_8 = 6/8\omega_p$.

Results given in Figure 2 indicate the coincidence of signals obtained by two different methods within the chaotic regime and we further use FDM only.

D. Charts of vibrations

The developed algorithms allow for analysis of the time histories $(w(0.5,t),\ w(x,t)x \in [0,1])$, power spectra, phase portraits $(w(\dot{w}),w(\dot{w},\ddot{w})$ for any point of the space co-ordinate x), Poincaré map $(w[w(t),w(t+T)])$, as well

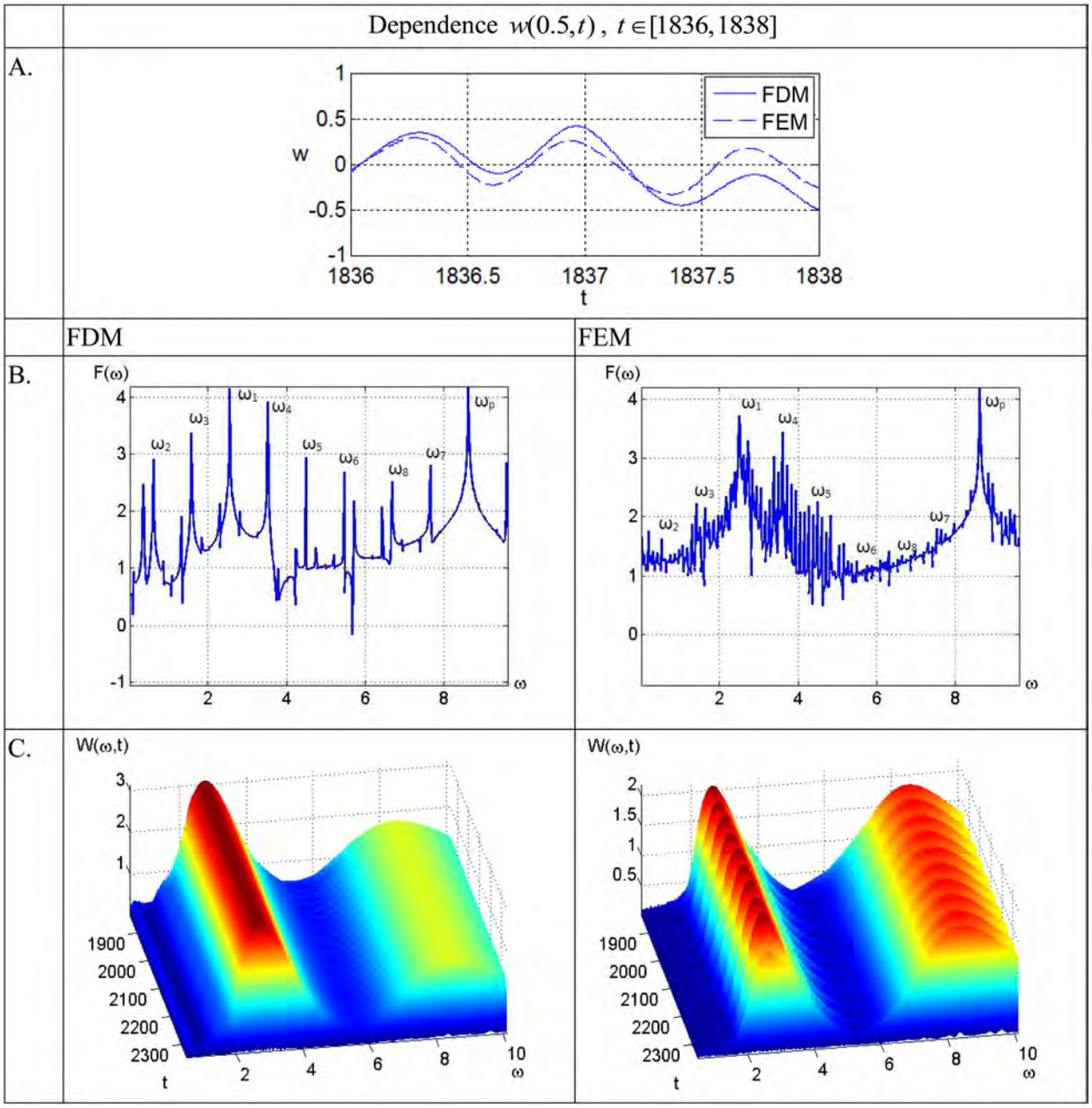

FIG. 2. Checking reliability of numerical results.

as the Lyapunov exponents for any parameters of the set $\{q_0, \omega_p\}$. The results are collected in the form of the so called vibration type charts in the parameters plane q_0, ω_p. Charts of the vibration regimes may serve as engineering recipes to keep the system dynamics in the required (safe) regime. However, first we have to determine the optimal value of nodes number (n) of the spatial co-ordinate, and a suitable number of partition of both excitation frequency (ω_p) and excitation amplitude (q_0) ($n_1 \times n_2$).

Fundamental notation of the beam vibration regimes versus control parameters $\{\omega_p, q_0\}$ for the spatial co-ordinate partition $n = 40$, $n = 80$, and $n = 120$ is given in Figure 3.

However, results yielded by the chart are not sufficient to validate convergence of the number of partitions (n) of the spatial co-ordinate. In order to remove this drawback, we are going to analyze the system for the following fixed parameters: $\varepsilon = 1$, $\omega_p = 8.625$, $q_0 = 59\,000$, where the system exhibits chaotic dynamics. This is approved by the constructed charts (a point with co-ordinates $(n_1; n_2) = (250; 59)$, $(\omega_p, q_0) = (8.625, 59\,000)$).

Figure 4 gives time series (1st row), the Fourier power spectra (2nd row), Poincaré maps $w_t(w_{t+T})$ (3rd row), deflection changes $w(x \in [0, 1], t)$ (4th row), 2D Morlet (5th row) wavelet spectra for $n = 40, 60, 80, 120$ partitions regarding the spatial co-ordinate $x \in [0, 1]$ obtained by FDM. An increase of number n implies a solution to the ODEs of the order 160, 240, 320, and 480 on each of the computational step. Time step has been chosen via the Runge principle. Analysis of the results indicates that by increasing n while dividing interval $x \in [0, 1]$, we may achieve convergence of the solution not only with respect to the average Fourier spectrum but also through other system characteristics like the time series and the Morlet wavelets. The so far obtained results validate the applied numerical approach used for solution of the studied beam, i.e., the system with infinite degrees of freedom, since a further increase of the beam partitions number of interval $x \in [0, 1]$ does not change the results. Here, the following frequency relations have been detected: ω_1, ω_p—independent, $\omega_2 = 7/8\omega_p$, $\omega_3 = 3/2\omega_1$, $\omega_4 = 2\omega_1$, $\omega_5 = 5/2\omega_1$, $\omega_6 = 3\omega_1$, $\omega_7 = 1/8\omega_p$, $\omega_8 = 6/8\omega_p$.

Note that the wavelet transform belongs to one of the most effective tools for the analysis of dynamic systems, and after checking other wavelets like Gauss 1, Gauss 8, Mexican hat vs. Morlet wavelet, the latter one is more

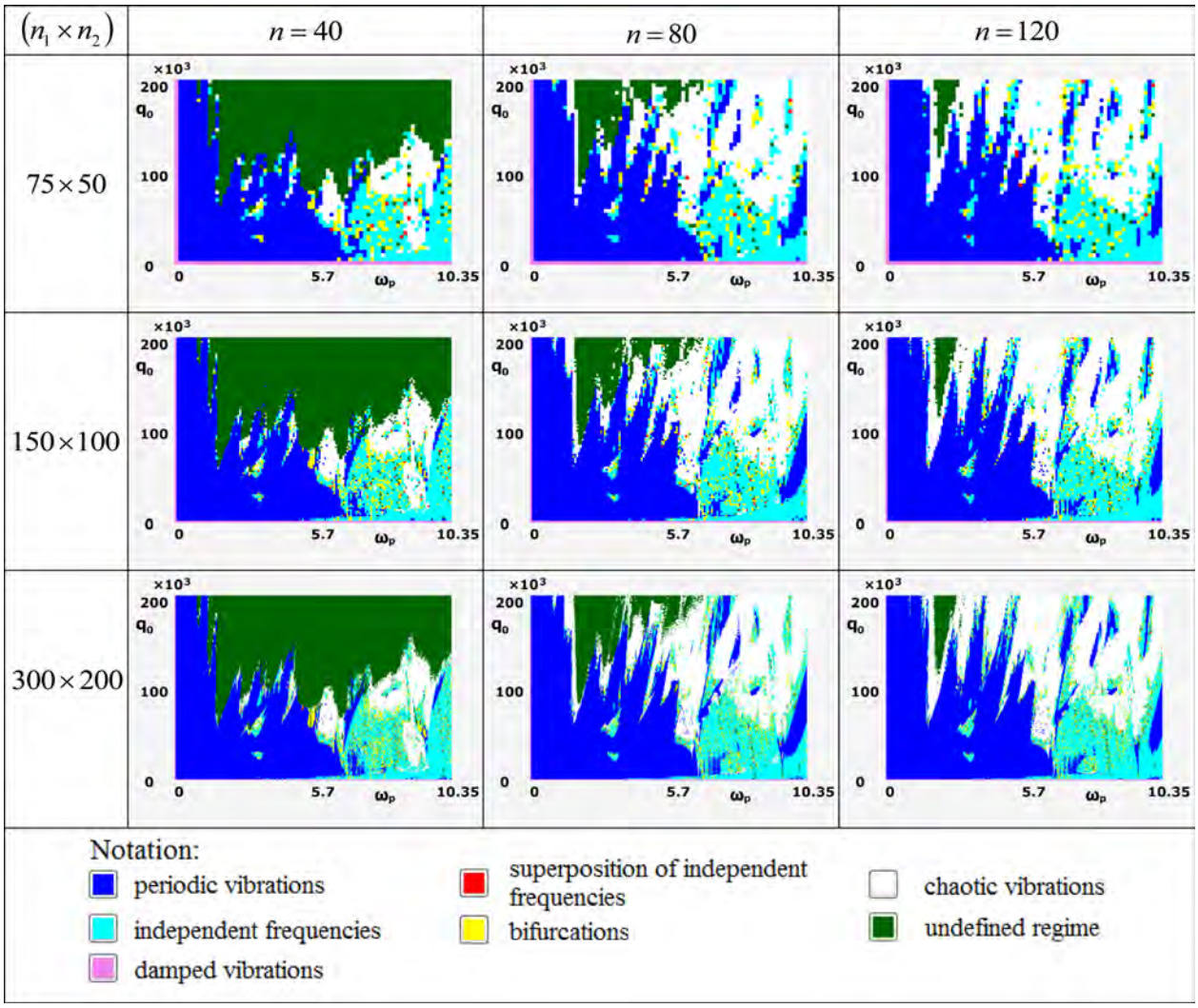

FIG. 3. Applied vibration type charts.

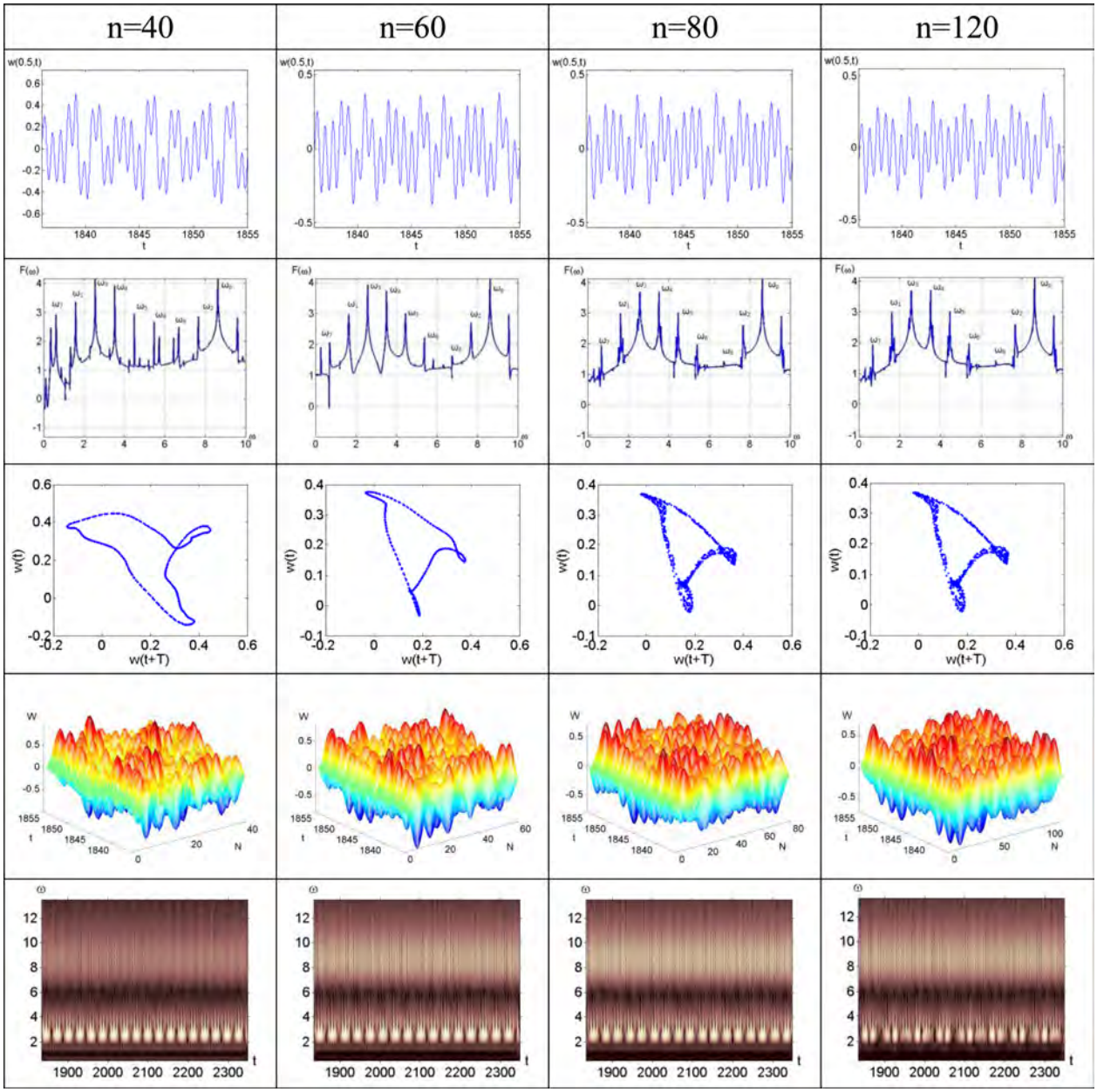

FIG. 4. Time series, power spectra, Poincaré maps, and wavelets for different n.

suitable for the investigation of beam vibrations, and has been further applied.

For further study, we take the following parameters: FDM of the second order accuracy; charts resolution $(n_1 \times n_2)$ are taken as 300×200; the number of partitions—$n = 120$. We address here the following query: Is the fourth-order Runge-Kutta method sufficient in getting the reliable results? We apply (for the pinned support) the sixth-order Runge-Kutta method (Butcher's method). Figure 5 gives a comparison of results obtained via two different algorithms for the following

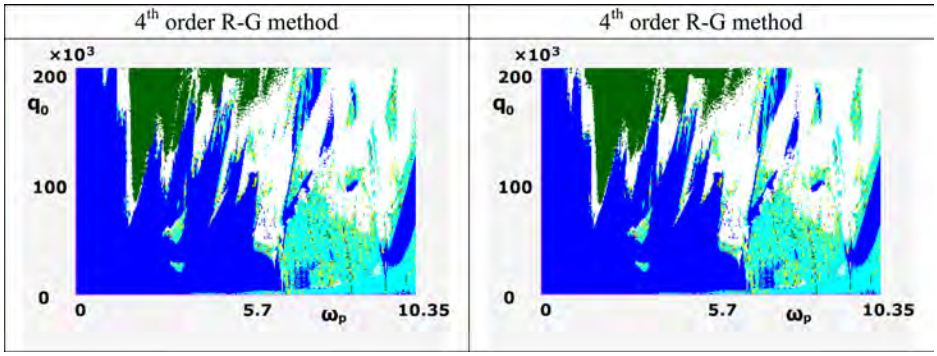

FIG. 5. Charts obtained through different Runge-Kutta methods.

fixed parameters: $n = 80,\ \lambda = 50,\ \varepsilon = 1,\ \omega_p = [0; 10.35)$, $q_0 = [0; 2 \times 10^5)$.

One may conclude that although the obtained results coincide, one needs 1.5-2 longer computational time in the case of application of the sixth-order Runge-Kutta method. Therefore, the fourth Runge-Kutta method is used further on.

IV. COMPUTATION OF LYAPUNOV EXPONENTS

A. Benetin's algorithm

The Lyapunov exponents characterize stability of dynamic systems in a phase space. A mathematical background for the existence of exponents gives the multiplicative ergodic Oseledec theorem[40,41] valid for the lumped mechanical systems. However, it cannot be applied directly to a continuous system. Schaumlöffel[42] addresses the concept of generalization of the theorem of Lyapunov exponents for the case of an infinite dimensional phase space. In order to get an approximate solution, one may reduce the problem to that of a finite system using the truncated number of ODEs. In the latter case, we get well defined Lyapunov exponents.

In this work, we study a dissipative continuous system which exhibits attractor compression during its evolution. Therefore, its attractor can be embedded into a so called iteration manifold with the finite dimension.[42] It means that its dynamics can be described via ODEs, which allow us to compute the Lyapunov exponents of the studied continuous system with infinite degrees of freedom. There is no practically realized procedure for the computation of inertial manifolds. Yang *et al.*[43] showed that it was possible to find directions of active system tangential dynamics sufficient for the description of the whole dynamics on a chaotic attractor. On the other hand, a set of finite active directions stand for the choice of local basis of the inertial manifold.

In this work, we apply the generalized Benettin's algorithm[41] with a simultaneous application of the neural networks. It allows us to use only one most suitable system's co-ordinate. The proposed algorithm includes the following steps:

1. Computation of a suitable time delay on the basis of the co-ordinate choice.
2. Computation of embedding space dimension.
3. Pseudo-phase reconstruction of a trajectory via time delays.
4. Construction of the approximating neural network.
5. Teaching of the neural network for the successive vector prediction.

Repeating the so far described procedure M times, one may estimate λ as an average value of the quantities $\tilde{\lambda}_l$ obtained on each step. A neural network with the following properties is highly required:

- The network should be robust with respect to the input information given by real numbers.
- The network should be self-organized with respect to its learning (only input information is used to construct an output space of solutions).
- The network should have straight extension (all couplings go from input to output neurons).
- The network should exhibit dynamic couplings with respect to the setting of synapses (adjustment of synapses links takes place during the network learning ($dW/dt \neq 0$), where W are the weight network coefficients).

Let point x_0 belong to the attractor A of a dynamic system. We call the evolution trajectory of x_0 the base trajectory. We choose a positive ε sufficiently smaller than the attractor dimension. Furthermore, let us take an arbitrary perturbed point $\tilde{x}_0$ that the following equality is satisfied $\|\tilde{x}_0 - x_0\| = \varepsilon$. We consider the evolution of chosen points x_0 and $\tilde{x}_0$ within a small time interval T, and we denote the obtained points by x_1 and $\tilde{x}_1$, respectively. The vector $\Delta x_1 = \tilde{x}_1 - x_1$ is called the perturbation vector. This allows us to estimate the quantity λ

$$\tilde{\lambda}_1 = \frac{1}{T} \ln \frac{\|\Delta x_1\|}{\varepsilon}. \tag{14}$$

Time interval T is chosen in a way to keep the excitation amplitude lesser than the linear dimensions of the phase space non-homogeneity and dimension of the attractor itself. Consider the normalized perturbation vector $\tilde{x}_1' = x_1 + \Delta x_1'$. The so far described algorithm is applied to points x_1 and $\tilde{x}_1$ instead of points x_0 and $\tilde{x}_0$, respectively. Repeating the so far described algorithm M times, one may estimate λ as the average arithmetic value of quantities $\tilde{\lambda}_l$ obtained on each of the computational steps.

However, there are a few drawbacks of the proposed method:

(1) It takes longer computation time in comparison to the classical methods, since in order to keep the required accuracy a large number of learning iteration loops are expected.
(2) The achieved accuracy is usually smaller in comparison to the existing classical approaches.

However, there are the following advantages:

(1) The proposed method is very suitable to use for short time series.
(2) It works better in comparison to the classical approaches for noisy data, since their influence can be sufficiently reduced while learning of the neural networks.
(3) Only one input co-ordinate is sufficient for the computation of Lyapunov spectrum.
(4) The proposed algorithm yields the Lyapunov exponents for systems without knowledge of their governing equations which is similar to the Wolf algorithm.[44] We note that Benettin's algorithm does not make it possible to solve the latter task.

It is well known that one of the important issues while analyzing dynamic systems is a construction of the Poincaré maps and analysis of the Kaplan-Yorke dimension. Consider a certain part of a surface in the phase space (Poincaré section) located transversally to the system vector field. Let us generate a system trajectory from point x lying on the transversal direction. We assume that for a certain time instant the trajectory intersects the transversal surface for the first time, and we denote this point by y. The Poincaré map

associates point x with that of the first intersection y. If the trajectory generated by x never returns to the intersection surface, we say that the Poincaré map is not defined in that point.

Fractal dimension of an attractor in the phase space R^N can be estimated through the Lyapunov exponents. It is called the Kaplan-Yorke dimension D_{ky} and it is defined via the Kaplan-Yorke formula. Assume that the spectrum of Lyapunov exponents is known for the N-dimensional system (it is ordered in the following way: $\lambda_1 > \lambda_2 > ... > \lambda_N$). The sum of all exponents is negative due to the system dissipation. We consider first k spectrum exponents, where k is the largest number satisfying the condition

$$\sum_{i=1}^{k} \lambda_i \geq 0. \tag{15}$$

Note that the number of exponents includes also positive ones, all zero ones, and a certain part of negative ones in order to keep the non-negative sum. Since the sum of exponents defines the character of a local change of the element of a phase volume on the attractor, then the phase volume of dimension $k < N$ is not decreased on the average. An increase of the subspace dimension by 1 implies already a compression of the element volume

$$\sum_{i=1}^{k+1} \lambda_i < 0. \tag{16}$$

Therefore, one may assume that the attractor dimension is within the interval $k \leq D_{ky} \leq k+1$. On the other hand, we may assume that the movement on the attractor is physically recognized as the stationary process, and hence

$$\lambda_1 + \lambda_2 + \cdots + d\lambda_{k+1} = 0. \tag{17}$$

Here, d stands for the fractional part of dimension. The full Kaplan-Yorke attractor dimension consists of a sum of integer k and fractional d parts

$$D_L = k + d = k + \frac{\sum_{i=1}^{k} \lambda_i}{|\lambda_{k+1}|}. \tag{18}$$

V. SCENARIOS TO CHAOS

A. Introduction

In the last years, the problem devoted to chaotic dynamics of continuous systems belongs to challenging tasks. It is associated with the investigation of Ginzburg-Landau equations,[45–48] multi-dimensional models of radio-physics systems describing coupled oscillators and generators,[49,50] as well as chains of oscillators and generators.[51–55] Majority of the works address the problem of finite dimension investigation of infinite dimensional (original) systems.

On the other hand, an important role in the continuous systems chaotic behavior plays their correspondence to the approximations via only a few degrees of freedom, regarding the attractors dimension, a number of the positive Lyapunov exponents and the Kolmogorov-Sinai entropy.

In the case of an additional positive Lyapunov exponent a novel unstable direction appears on the system trajectory, and hence its dynamics should be qualitatively changed. However, the Lyapunov dimension defines the average dimension of the attractor local volume which is conserved, i.e., neither compressed nor extended. It is known that while defining the Lyapunov dimension we take into account the positive, zeroth, and negative exponents. The latter ones only influence the metric system properties rather than its nonlinear dynamics (see Ref. 43).

B. From periodicity to chaos and hyper-chaos

In this section, we consider transitions into chaos for the pinned flexible beams. A pinned flexible beam is subjected to the action of the uniformly distributed periodic load $q = q_0 \sin(\omega_p t)$ for $\delta = \frac{l}{h}$. Its scenarios of transition from regular to chaotic dynamics are reported in Figures 6–16. Cells of those figures include the following characteristics: (a) signal $t \in [1836; 1855]$; (b) Fourier power spectrum; (c) phase portrait; (d) deflection in time instant $t = 1836$; (e) deflection $w(x,t)$, $x \in [0; 1]$, $t \in [1836; 1855]$; (f) pseudo-Poincaré map; (g) phase portrait (neural network); (h) Lyapunov exponents; (i) 2D Haar wavelets; (j) 2D Morlet wavelets; (k) 3D Haar wavelets; and (l) 3D Morlet wavelets.

We discuss the results shown in Figures 6–16.

1. The amplitude of excitation $q_0 = 0.125 \times 10^3$ corresponds only to one frequency $\omega_p = 6.9$ in the Fourier power spectrum. An increase of the excitation amplitude up to $q_0 = 0.5 \times 10^3$ yields the occurrence of independent frequency $\omega_1 = 0.63$, which is also visible in the associated wavelets and has a rather small magnitude. All Lyapunov exponents are negative which means that the Kaplan-Yorke dimension is zero and the KS entropy (h) is negative. Both time history and beam vibrations are symmetric in a fixed time instant. All mentioned characteristics validate the signal periodicity. Compression of the phase volume (d) is rather large and negative.
2. An increase of the excitation amplitude up to $q_0 = 4 \times 10^3$ wakes up the first dependent frequency $\omega_2 = 5.64$, which satisfies the formula $\omega_2 = \omega_p - 2\omega_1$. This frequency is also visible on the Morlet wavelets, but owing to its small value it is hardly recognized through the Haar wavelets. The first Lyapunov exponent and the Kaplan-Yorke dimension become positive, and the KS entropy becomes positive and equal to the value of the first Lyapunov exponent. A small deviation from the previous full symmetry is noted regarding the time series and beam vibrations in the fixed time instant. The phase portrait shows the attractor as a collection of a few rings. The phase compression coefficient is decreased. The system starts to approach chaos.
3. Load amplitude $q_0 = 5 \times 10^3$ awakes the frequency $\omega_3 = 1.89$ which is defined via the ratio $\omega_3/\omega_1 = 3$. The wavelets exhibit an increase of the amplitude of frequency ω_2, but still it is not possible to identify ω_3. Phase space orbits are remarkably divergent. Two of the Lyapunov

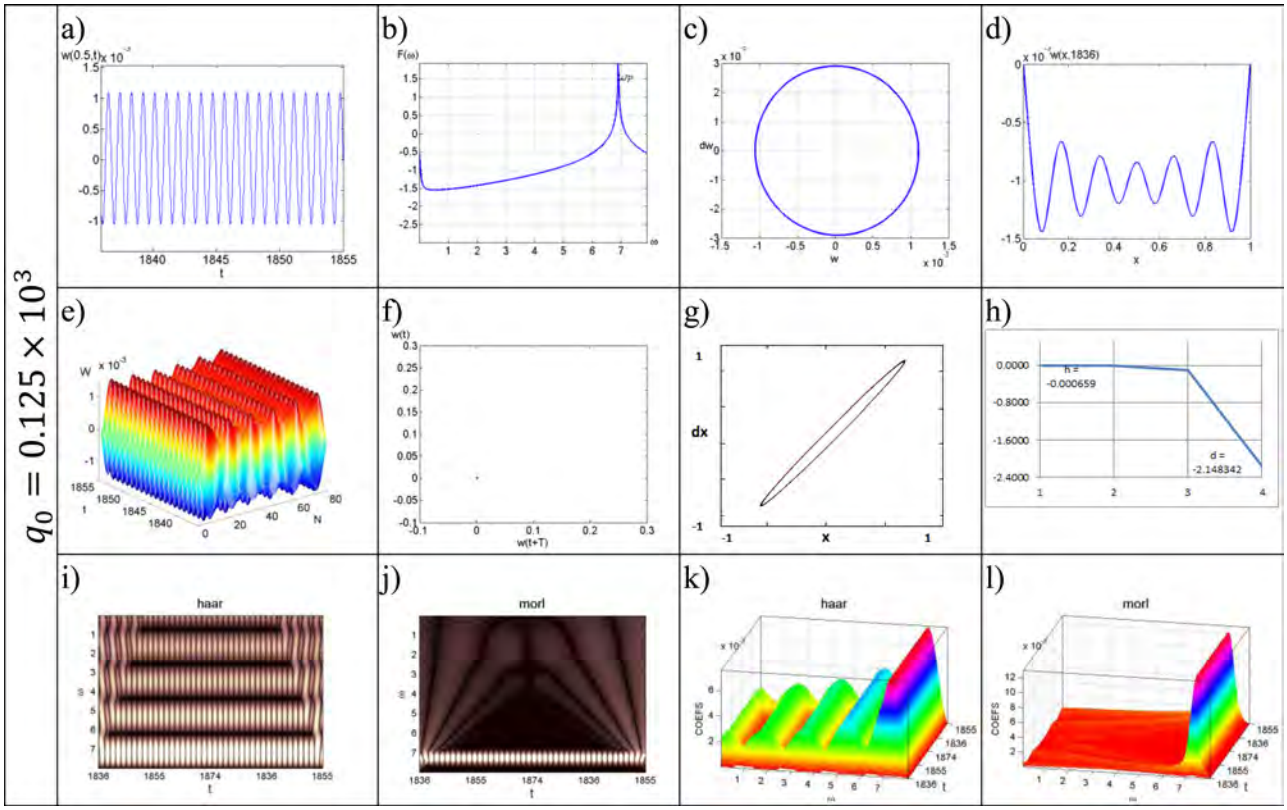

FIG. 6. Beam characteristics for $q_0 = 0.125 \times 10^3$.

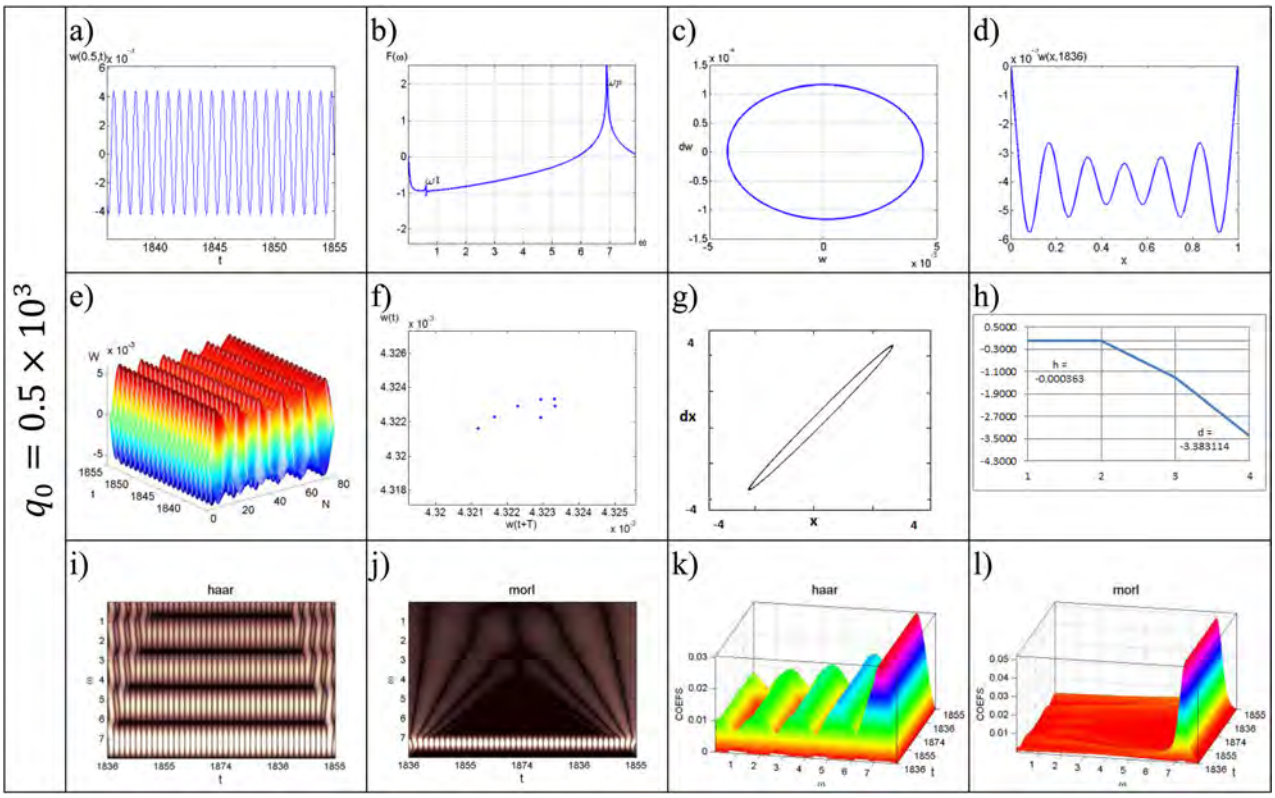

FIG. 7. Beam characteristics for $q_0 = 0.5 \times 10^3$.

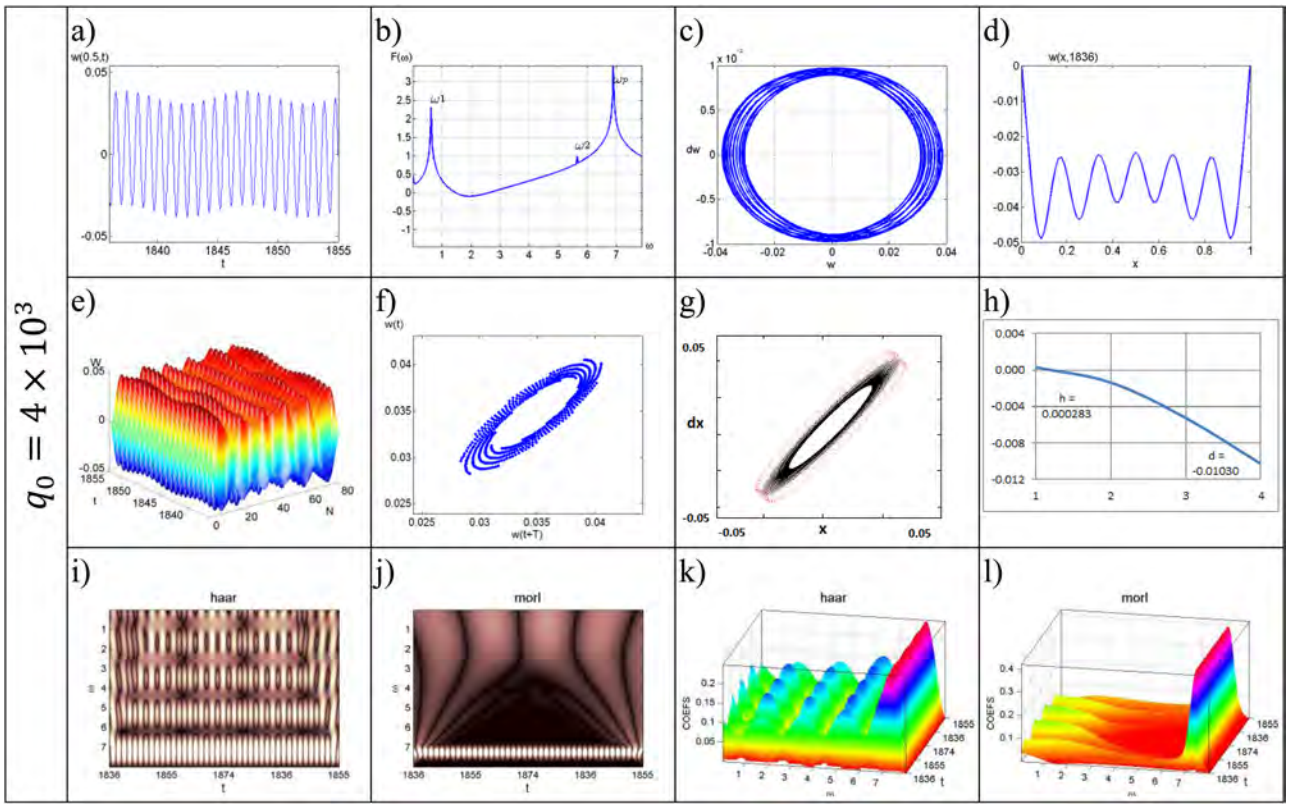

FIG. 8. Beam characteristics for $q_0 = 4 \times 10^3$.

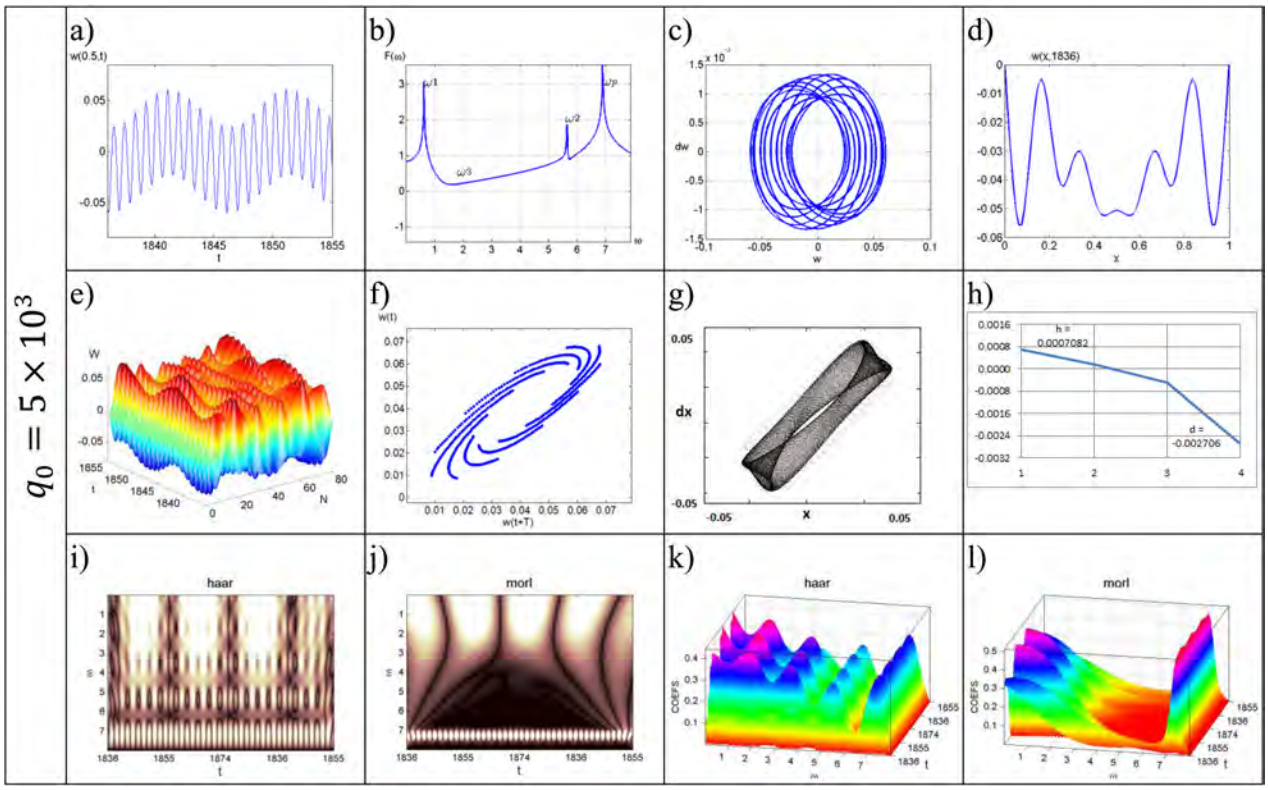

FIG. 9. Beam characteristics for $q_0 = 5 \times 10^3$.

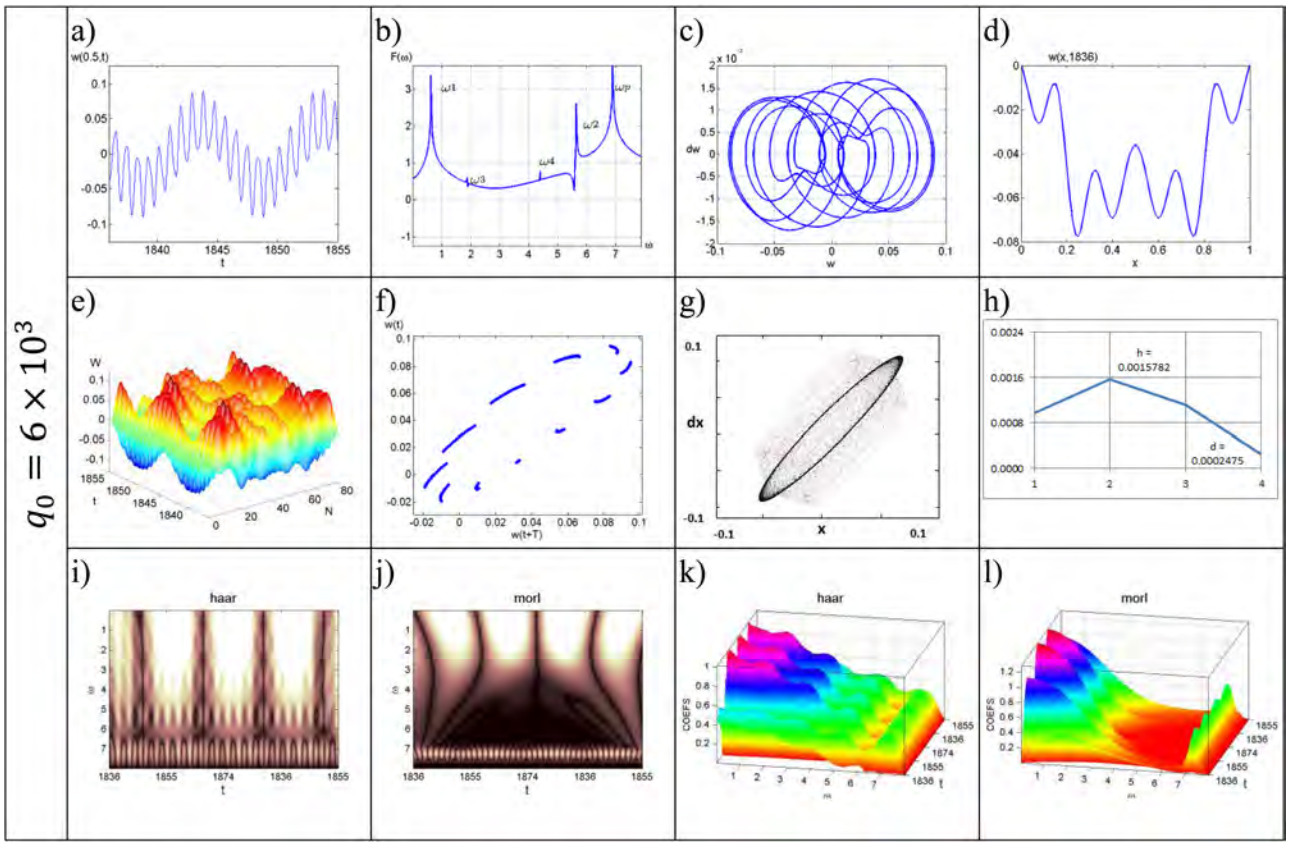

FIG. 10. Beam characteristics for $q_0 = 6 \times 10^3$.

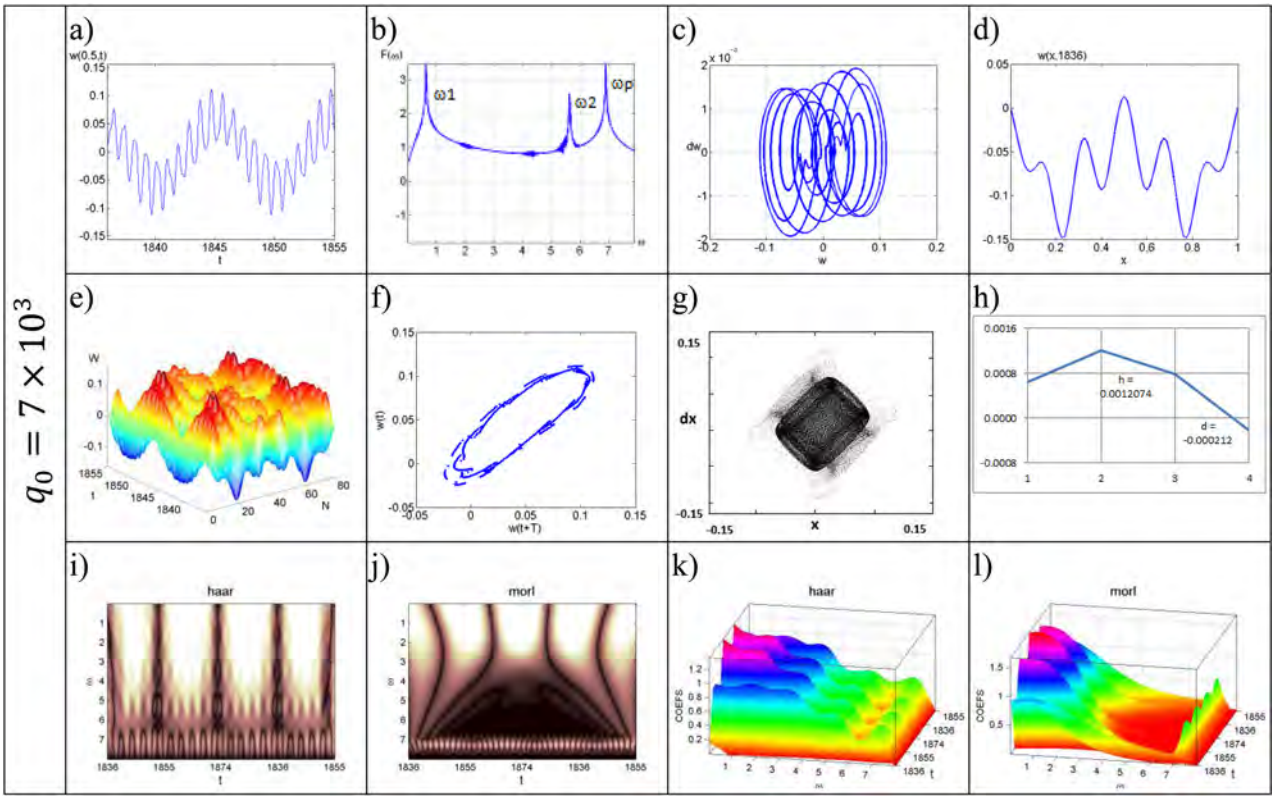

FIG. 11. Beam characteristics for $q_0 = 7 \times 10^3$.

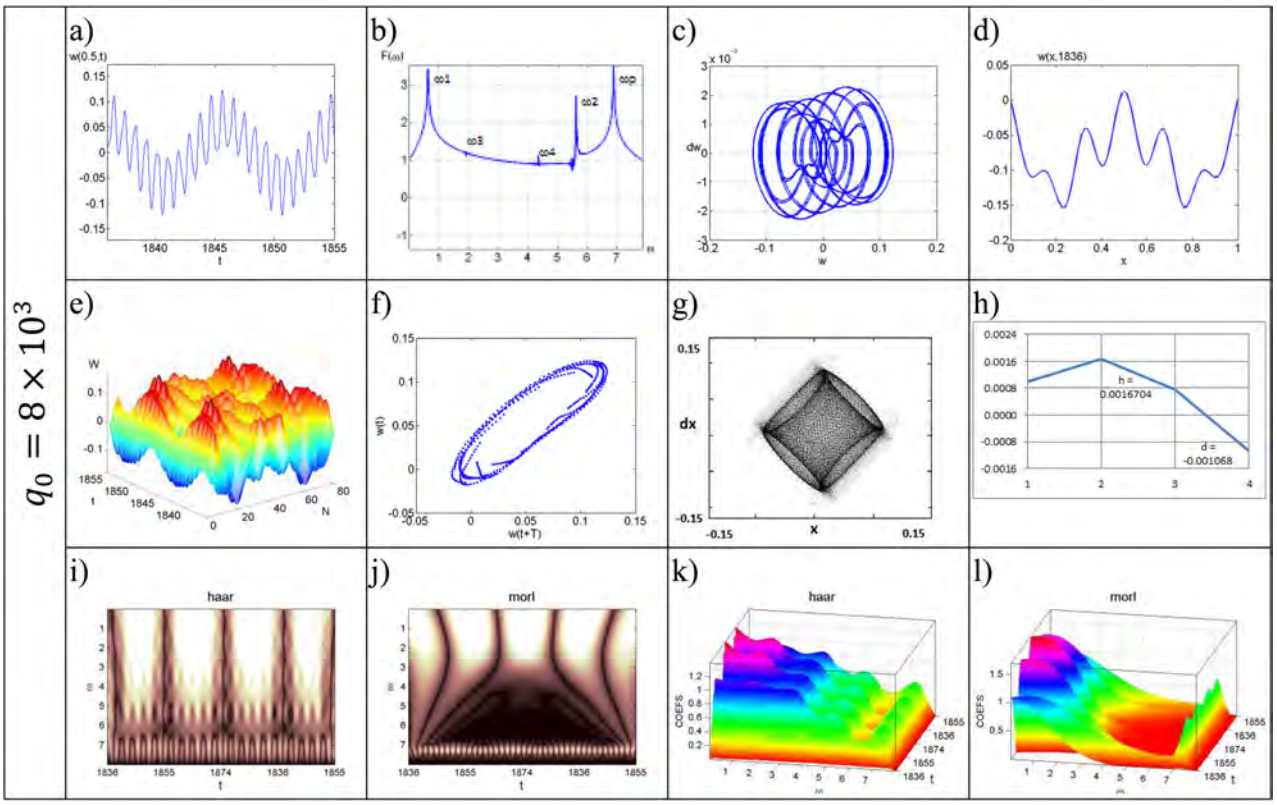

FIG. 12. Beam characteristics for $q_0 = 8 \times 10^3$.

exponents are positive and the Kaplan-Yorke dimension is increased. The KS entropy achieves its maximum value for the second Lyapunov exponent, and it is large in comparison to the load $q_0 = 4 \times 10^3$. The phase portrait exhibits a torus. Although the phase volume compression increases, it still remains negative. This illustrates a higher chaotic intensity of the flow, and the system approaches the chaos-hyper chaos state.

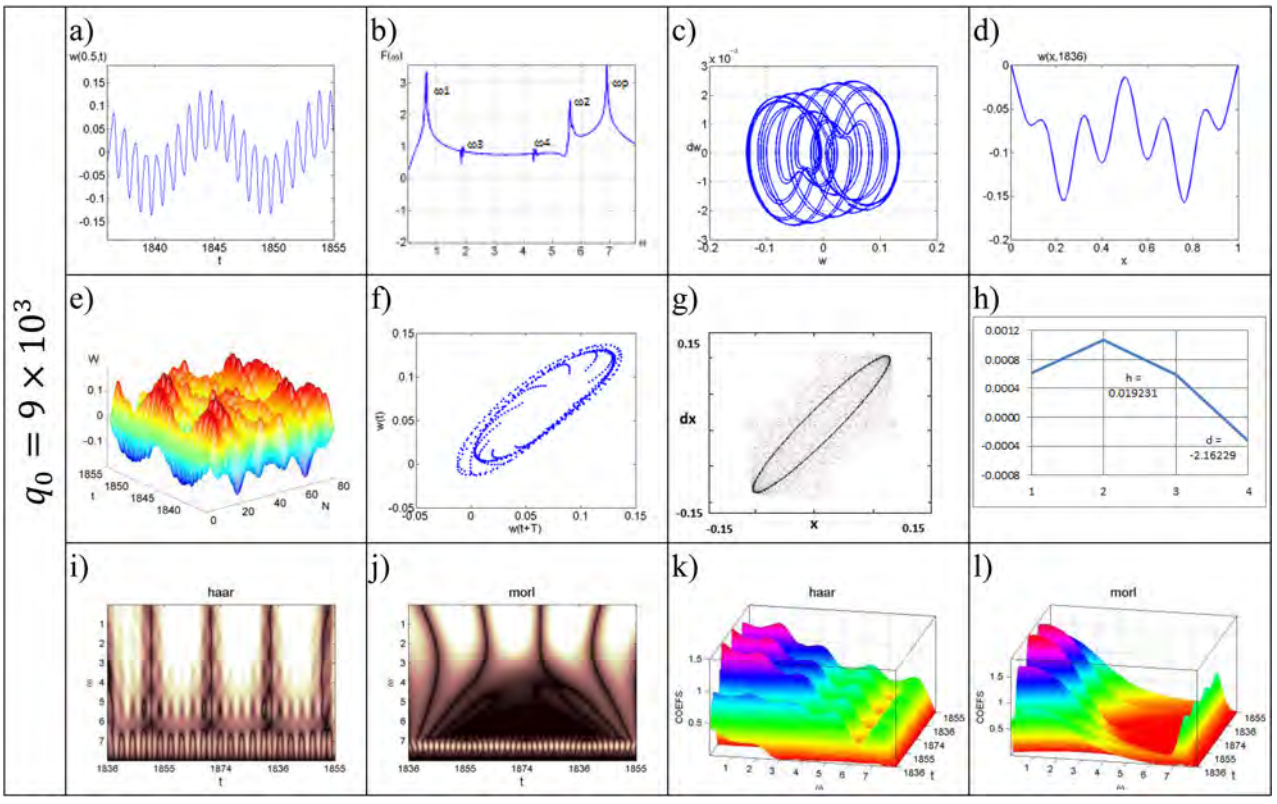

FIG. 13. Beam characteristics for $q_0 = 9 \times 10^3$.

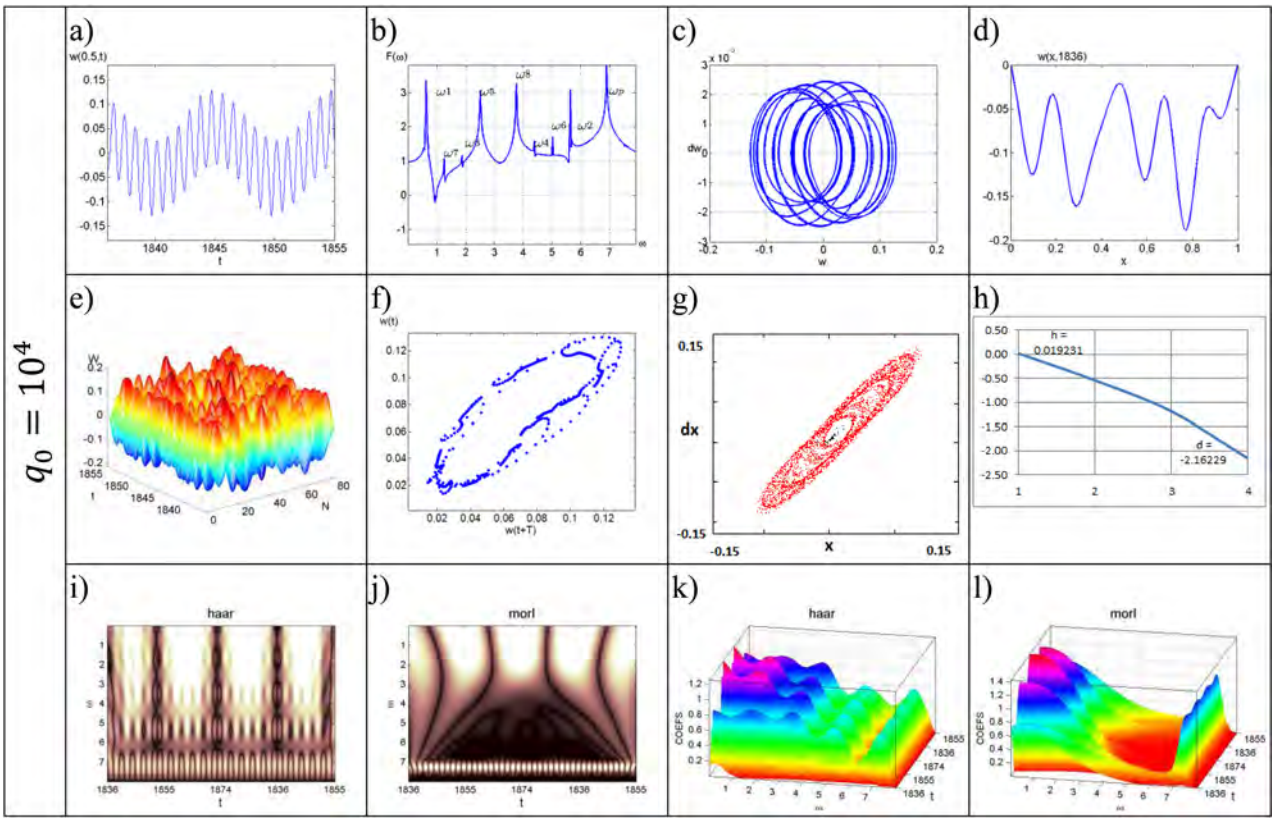

FIG. 14. Beam characteristics for $q_0 = 10^4$.

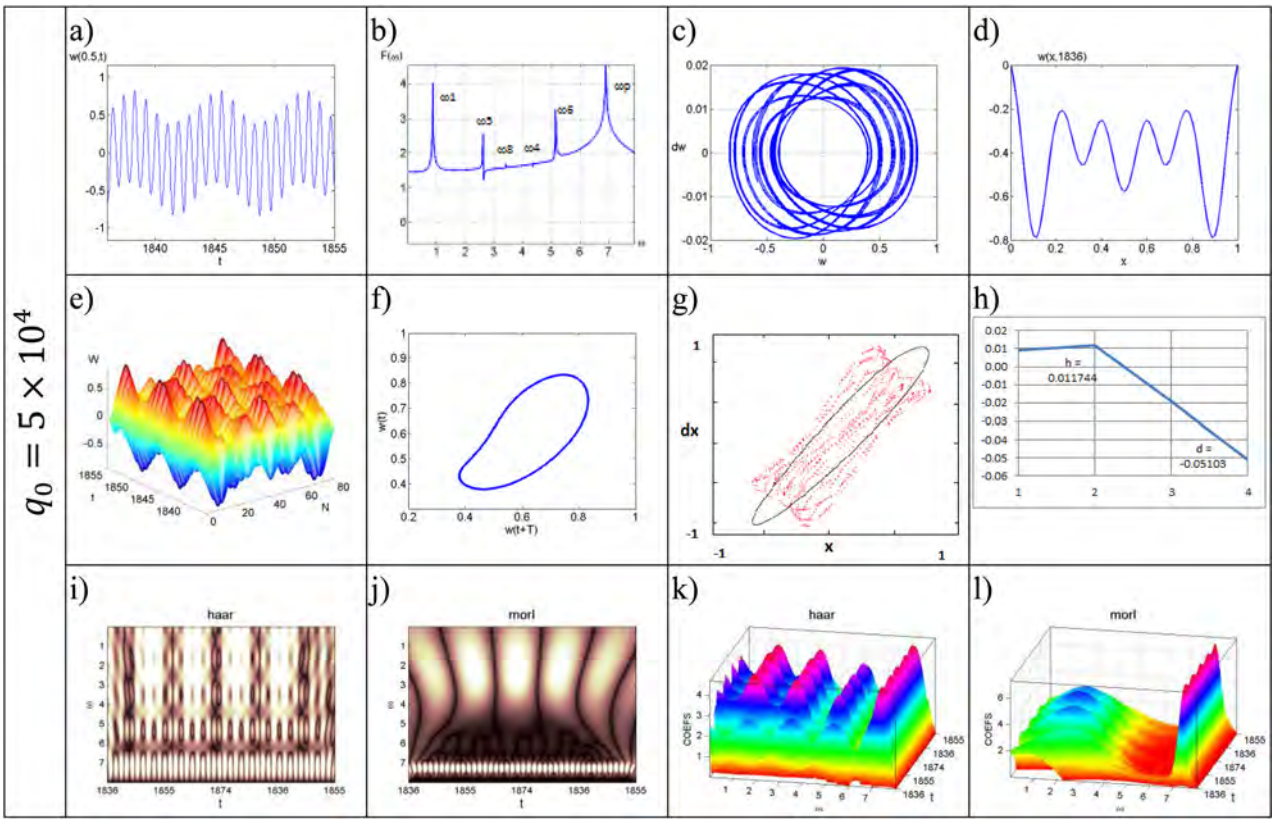

FIG. 15. Beam characteristics for $q_0 = 5 \times 10^4$.

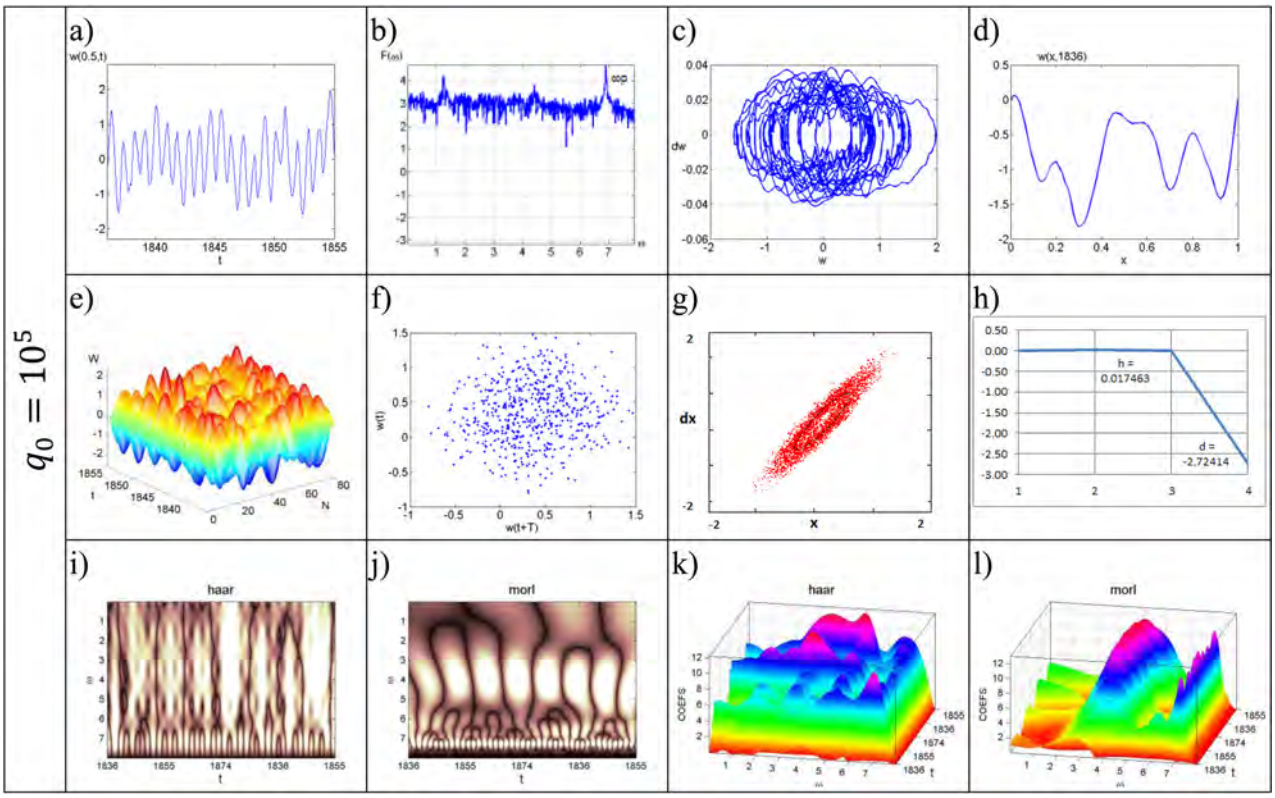

FIG. 16. Beam characteristics for $q_0 = 10^5$.

4. When the load achieves $q_0 = 6 \times 10^3$ the new frequency occurs $\omega_4 = \omega_2 - 2\omega_1 = 4.38$. The Lyapunov exponents and the Kaplan-Yorke dimension increase comparing to the previous state. The KS entropy value and the phase space compression become positive. Both Haar and Morlet wavelets exhibit slightly the frequencies ω_3 and ω_4, but their amplitudes are small which is also approved by the Fourier power spectra. The phase portrait tends to a planar ring structure with a simultaneous collapse. Beginning with a certain time instant the system starts to pulsate which is also validated by the phase portrait and Lyapunov exponents. In other words, the system is in the chaos-hyper-chaos regime.
5. Load amplitudes $q_0 = 7 \times 10^3$ and $q_0 = 8 \times 10^3$ do not change the system chaotic level. The Lyapunov exponents are slightly decreased for $q_0 = 7 \times 10^3$, and then they increase again to their previous level. Both the phase volume compression and RS entropy are changed (for $q_0 = 7 \times 10^3$ they decrease, but for $q_0 = 8 \times 10^3$ they increase again). The Kaplan-Yorke dimension as well as the amplitudes of frequencies ω_3 and ω_4 is increased (in both the power spectrum and Haar and Morlet wavelets). Then, signal asymmetry is increased. Although the phase portrait again loses its ring structure, the attractor becomes more ordered. The system still remains in the chaos-hyper-chaos state.
6. Load amplitude $q_0 = 9 \times 10^3$ yields a collapsed ring structure. The Lyapunov exponents become smaller. The amplitudes of frequencies ω_3 and ω_4 are still increasing. Here, a transition from chaos-hyper chaos state into chaos is observed which is also validated by essential changes of the Poincaré maps.
7. A further increase of load amplitude up to $q_0 = 10 \times 10^3$ causes the occurrence of independent frequencies that satisfy the relations: $\omega_6 = 2\omega_5 = 5.02$, $\omega_5 = 2\omega_7 = 2.5$, $\omega_8 = 2\omega_3 = 3.78$. Both Haar and Morlet wavelets are noisier, but in the Haar wavelets the separable frequencies cannot be practically distinguished. Only the first Lyapunov exponent is still positive, but its magnitude is by two orders higher than its previous values. Again, the magnitude of KS entropy coincides with the value of the first Lyapunov exponent. Orbits are more broad-banded and the geometric attractor structure is not clearly defined. Beam vibrations and time series exhibit large asymmetry. However, the load amplitude $q_0 = 50 \times 10^3$ forces the system to exhibit small developed chaotic regime in comparison to its previous chaotic state which is recognized through the phase portrait. The time series asymmetry is decreased. Two first Lyapunov exponents become positive and the magnitude of the first exponent is by one order smaller than that corresponding to the load $q_0 = 10 \times 10^3$. The Kaplan-Yorke dimension is lesser than that regarding the loading amplitudes $q_0 = 6 \times 10^3$ to $q_0 = 9 \times 10^3$. The KS entropy value is now equal to the value of the second Lyapunov exponent and remains relatively large. The Fourier spectrum exhibits the lack of frequencies ω_7, ω_8, and ω_2, which is also validated by both wavelets. Time history remains symmetric again, and the beam vibrations monitored in an arbitrary time instant have rather small asymmetry. It means that the system is withdrawn from its previous deep chaotic state.
8. Finally, the system approaches a deep chaos regime whose power spectrum is reported for the load amplitude

$q_0 = 100 \times 10^3$. Time series and beam vibrations exhibit the largest asymmetry, whereas the Lyapunov exponents achieve the highest values comparing to all previous illustrated cases. The phase portrait does not have a clear geometric structure. Wavelets versus time consist of a non-homogeneous structure regarding all frequencies.

9. Equations (1) are strongly non-linear PDEs, where the function of beam deflection w(x,t) and beam displacement u(x, t) depends both on time and spatial co-ordinate, and it is tempting to expect spatial chaos in spite of timing chaos occurrence, i.e., the beam should exhibit chaotic deflection changes along the length $x \in [0;\ 1]$ and time. In previous points 1–8, we have illustrated a scenario of changes of beam vibrations versus time. In the input equations, the function w and its derivatives clearly express physical meanings of the beam vibrations: $w(x,\ t)$—beam deflection, $w'_x(x,\ t)$—tan of an angle of a tangent to the beam deflection curve in points, where the derivative $w''_{xx}(x,\ t)$ is estimated. Since the latter one yields an approximate formula governing the beam curvature shape along its length, those functions can be understood as modal characteristics of changes of the beam surface in time. This characteristic extends the classical plane phase concept to its 3D version, since $w(x,t)$, $\dot{w}_t(x,\ t)$ and $\ddot{w}_{tt}(x,t)$ describe the beam deflection, velocity and acceleration, respectively. In order to study the space chaos, one may follow windows (e) reported in Figures 6–16. A transition into chaos is associated with serious and remarkable changes of the beam surface. Furthermore, these changes include simultaneous transition from symmetric to non-symmetric beam vibration states and vice versa. Fully developed chaos is reported in Figure 16. Changes of the Lyapunov exponents, the Kaplan-Yorke dimension illustrated in previous paragraphs, supplement the so far studied transition into the spatio-temporal chaos. It should be emphasized that the spatial chaos and timing chaos practically occur synchronously. Figure 4 illustrates results showing beam surface changes in time interval $t \in [1835;\ 1855]$ for different degrees of freedom of the beam model (partition of the interval $x \in [0;\ 1]$ into parts of $n = 40, 60, 80, 120$). This means that we do really monitor the spatio-temporal chaos exhibited by our beam, treated as a continuous system and not a lumped object modeled by a few degrees of freedom. Observe that the obtained results are validated and reliable, since the full coincidence of bending surfaces occurs for $n = 80$ and $n = 120$.

In Figure 17, the following characteristics are given: (a) Kaplan-Yorke dimensions, (b) Lyapunov exponents, (c) entropy h versus load amplitude q_0, (d) phase space compression d versus q_0.

Table I includes the values of the quantities regarding drawings of Fig. 17.

VI. ON THE SYMMETRIC AND NON-SYMMETRIC BEAM VIBRATIONS

We have already mentioned that when investigating chaotic vibrations of the harmonically excited flexible Euler-Bernoulli type beams with symmetric boundary conditions we detected a non-symmetric solution. However, this is possible to achieve under the assumption that we have either initial non-symmetric imperfections, non-symmetric initial vibration forms, or small errors due to numerical computations through the Runge-Kutta method. In the so far reported results, all of the mentioned initial imperfections have been symmetric and hence the non-symmetric solutions are yielded through the errors introduced by the Runge-Kutta methods. Namely, the previous step solution error is then

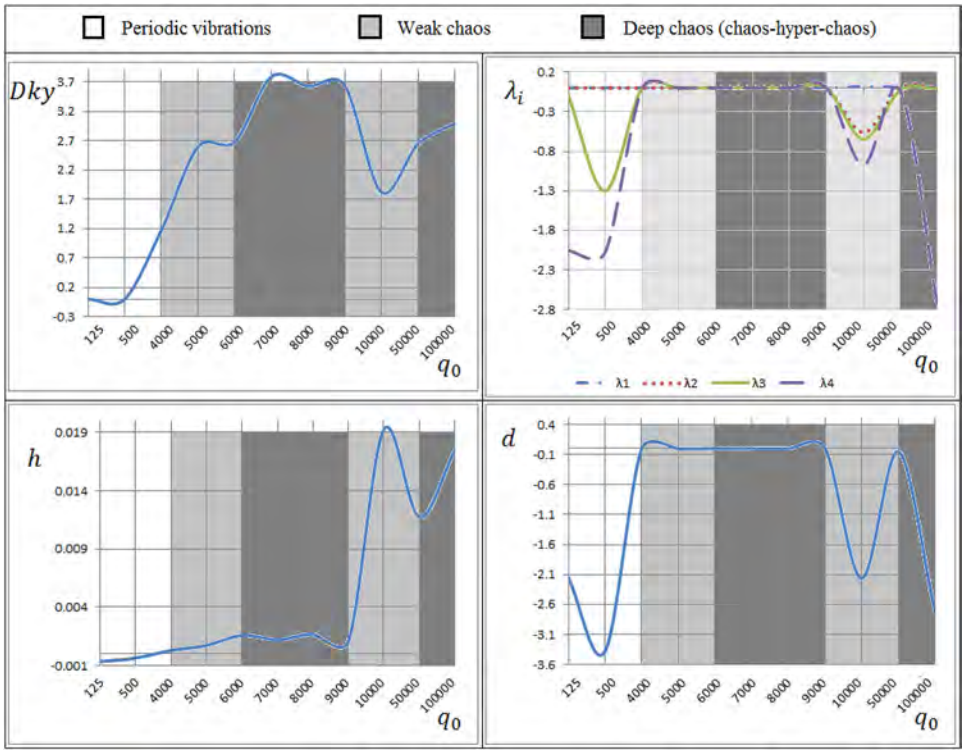

FIG. 17. Four beam vibration characteristics.

TABLE I. The values of λ, D_{ky}, h, and d.

q_0	125	500	4×10^3	5×10^3	6×10^3	7×10^3	8×10^3	9×10^3	10^4	5×10^4	10^5
λ_1	−0.0006599	−0.0003631	0.0002833	0.0007082	0.0009791	0.0006536	0.0009827	0.0006124	0.0192312	0.0090136	0.0138237
λ_2	−0.0005464	−0.0001815	−0.0016836	−0.0005367	0.0005991	0.0005538	0.0006877	0.0004597	−0.5624457	0.0027311	0.0036397
λ_3	−0.0911141	−1.3026389	−0.0038560	−0.0006610	−0.0004654	−0.0004171	−0.0009066	−0.0004892	−0.6462801	−0.0306106	−0.0114446
λ_4	−2.0560221	−2.0799312	−0.0050447	−0.0022174	−0.0008653	−0.0010024	−0.0018324	−0.0009136	−0.9727997	−0.0321723	−2.7301685
D_{ky}	0	0	1.168	2.594	2.681	3.788	3.627	3.638	1.824	2.645	3.002
h	−0.0006599	−0.0003631	0.0002833	0.0007082	0.0015782	0.0012074	0.0016704	0.0010721	0.0192312	0.0117447	0.0174634
d	−2.1483425	−3.3831147	−0.0103010	−0.0027069	0.0002475	−0.0002121	−0.0010686	−0.0003307	−2.1622943	−0.0510382	−2.7241497

transmitted to the next one which plays a crucial role while monitoring the beam chaotic dynamics. The obtained solution can be understood as the non-symmetric one. In order to get symmetric solutions, we have to preserve symmetry conditions. An increase of the partition points of interval $[0;1]$ and the use of the sixth-order Runge-Kutta method instead of the fourth-order one do not allow us to change the obtained results. It should be emphasized that asymmetry in the solution on each computational step plays here a key role.

An analogous effect can be achieved by an artificial introduction of the load areas located symmetrically with respect to the beam center with almost the same loading amplitudes. In other words, in order to validate the numerical simulation we need to preserve full coincidence of the solutions regarding the left and right hand sides of the studied space. This can be achieved by mapping one half of the space into the second one with appropriate signs on each step of the modeling process.

Next, we present a numerical experiment for the beam dividing the interval of $x \in [0;1]$ for $n = 80$, $\varepsilon = 1$, $\omega_p = 9$, $q_0 = 5\times10^4$. Experimental results are given in Fig. 18. One may recognize that in case (a), (b), and (c) the power spectra obtained using the FFT procedure coincide regarding the frequency values and they are divergent with respect to power.

The power spectra imply the following relations of the occurring frequencies: ω_p—independent frequency, $\omega_1 = 1/3\omega_p$, $\omega_{14} = 1/3\omega_p$, $\omega_2 = 3/18\omega_p$, $\omega_3 = 4/18\omega_p$, $\omega_4 = 6/18\omega_p$, $\omega_5 = 8/18\omega_p$, $\omega_6 = 9/18\omega_p$, $\omega_7 = 17/18\omega_p$, $\omega_8 = 14/18\omega_p$, $\omega_9 = 1/18\omega_p$, $\omega_{10} = 2/18\omega_p$, $\omega_{11} = 5/18\omega_p$, $\omega_{12} = 7/18\omega_p$, $\omega_{13} = 10/18\omega_p$, $\omega_{15} = 13/18\omega_p$, $\omega_{16} = 15/18\omega_p$, $\omega_{17} = 16/18\omega_p$.

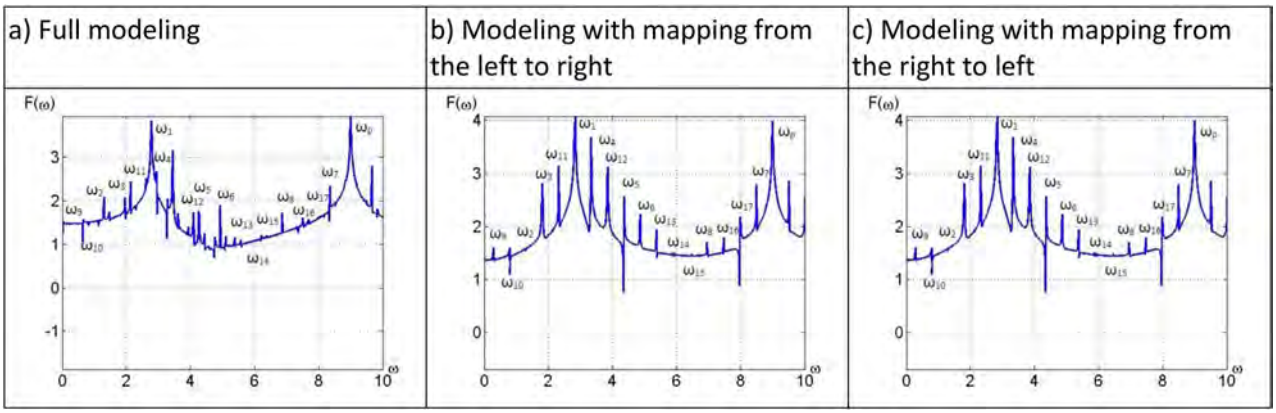

FIG. 18. Power spectrum.

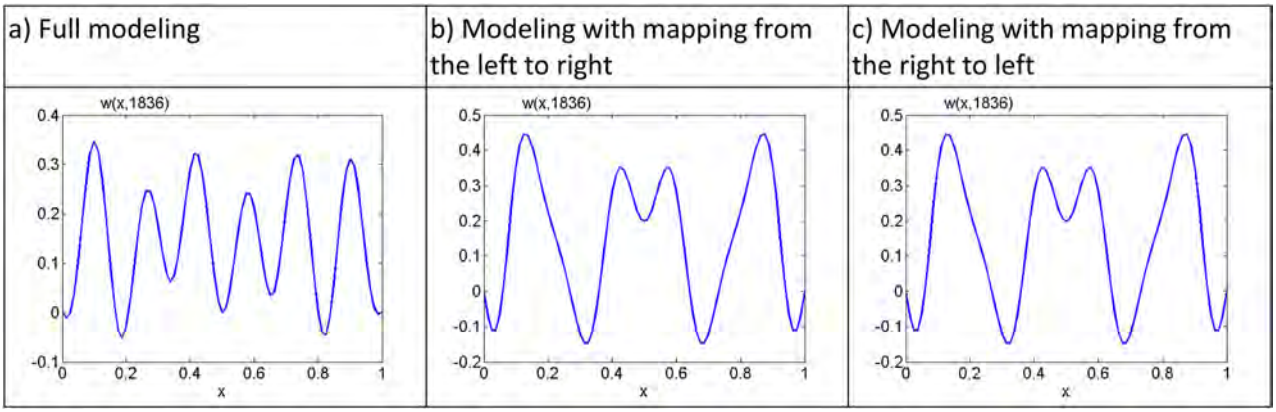

FIG. 19. Beam deflection versus x.

Figure 19 gives beam deflections versus x obtained for the time instant $t = 1836$. Solutions marked by (b) and (C) fully coincide and they are symmetric, whereas solution (a) is non-symmetric.

Figure 20 shows vibration type charts for the following fixed parameters $\lambda = 50$, $\varepsilon = 1$, $\omega_p = [0; 10.35)$, $q_0 = [0; 2 \times 10^5)$ for either symmetric or non-symmetric stability loss for $n = 40$, $n = 60$, $n = 80$, $n = 120$.

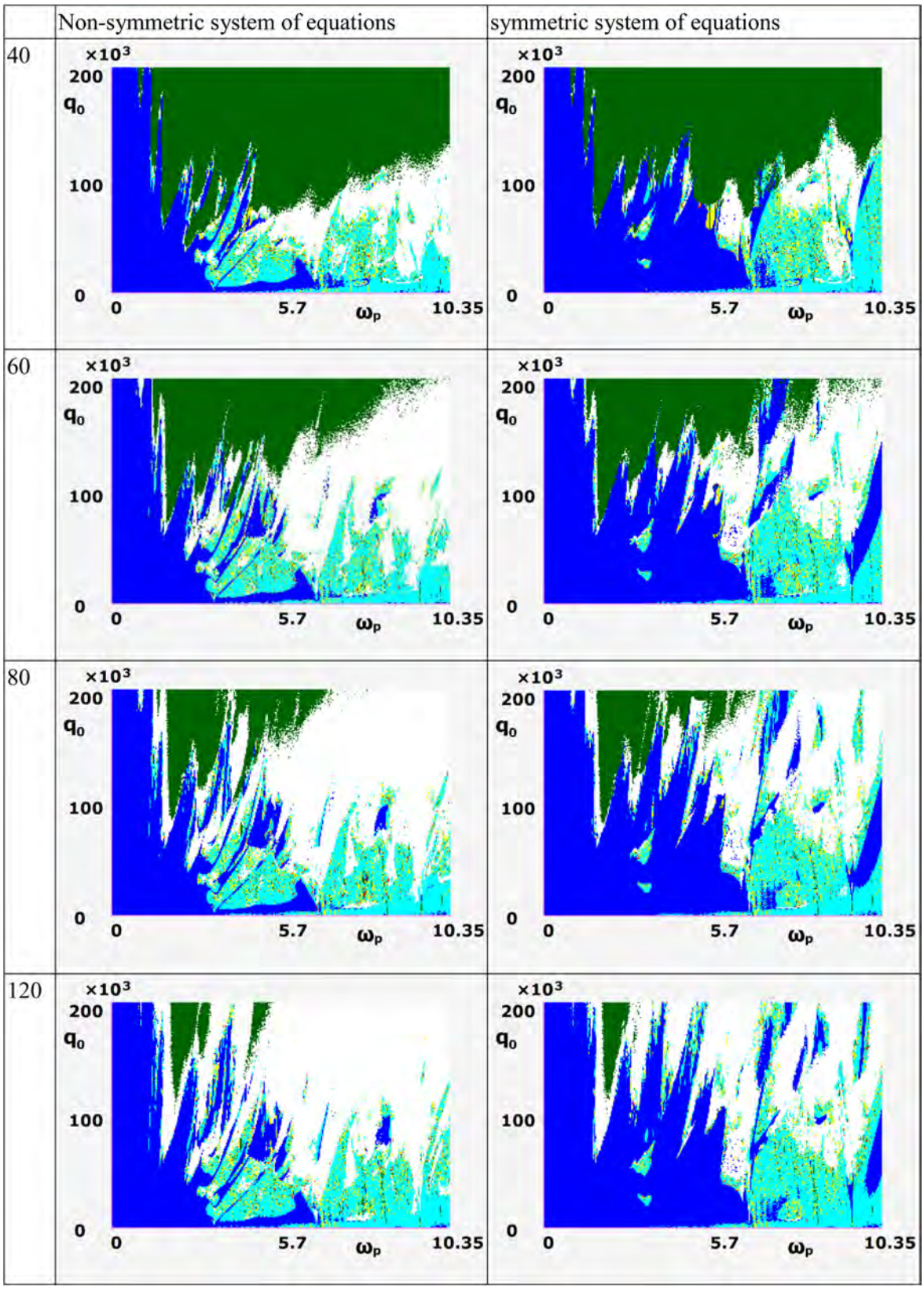

FIG. 20. Vibration charts for non-symmetric and symmetric set of equations.

VII. CHAOS VERSUS λ AND BOUNDARY CONDITIONS

Figure 21 includes the vibration type charts with the control parameters $n = 120$, $\omega_p = [0; 10.35)$, $q_0 = [0; 2 \times 10^5)$ for different boundary conditions (pinned support on both ends, hinged support, and fixed support) and different beam thickness ($\lambda = 50$ and $\lambda = 100$). In the case of symmetric boundary conditions, the vibration regimes almost coincide for small and average frequencies. In the case of non-symmetric pinned-fixed supports, the symmetric forms are obtained only for small frequencies.

Non-symmetric type of support is associated with a larger domain of chaotic vibrations. A decrease of the beam thickness causes an increase of the periodic beam vibrations with respect to the areas of amplitude and frequency of harmonic excitation.

VIII. THE INFLUENCE OF EXCITATION FREQUENCY

We take the pinned beam with $q_0 = 10^5$, $\varepsilon = 1$, $\lambda = 50$ and we monitor its vibrations versus excitation frequency. Computational results given in Figure 21 should be considered together with those presented in Figure 22(a). The excitation frequency (ω_p) essentially influences the beam vibration modes. In the case of periodic vibrations we may have one wave from $\omega_p = 1$(a) up to $\omega_p = 7$(a), and more. During the transition into chaos, the space-temporal chaotic vibrations are observed (bending surface exhibits changes in time in the chaotic manner $\omega_p = 6$, $\omega_p = 11$ (a)). In other words, the system transition in timing chaos implies its transition into temporal-space chaos. Transition into chaos can be realized through various scenarios. For instance, for $\omega_p = 8$(b) the Feigenbaum scenario takes place with clearly manifested four Hopf bifurcations.

Cells in Figure 22 include the following characteristics: (a) time series $w(x,t)$, $x \in [0;1]$, $t \in [1836; 1855]$; (b) Fourier power spectrum $w(0.25,t)$ for the time interval $t \in [1836; 2348]$; (c) phase portrait; (d) modal portrait; (e) pseudo Poincaré map; (f) autocorrelation function; (g) 2D Morlet wavelet; (h) 3D Morlet wavelet.

IX. SPATIO-TEMPORAL CHAOS EXHIBITED BY A CURVILINEAR EULER-BERNOULLI-BEAM

A. Mathematical model

Mathematical model of a curvilinear beam is described by the following system of non-linear non-dimensional PDEs:

$$\begin{aligned}
&\frac{\partial^2 u}{\partial x^2} - k_x \frac{\partial w}{\partial x} + L_3(w,w) - \frac{\partial^2 u}{\partial t^2} = 0,\\
&\frac{1}{\lambda^2}\left\{-\frac{1}{12}\frac{\partial^4 w}{\partial x^4} + k_x\left[\frac{\partial u}{\partial x} - k_x w - \frac{1}{2}\left(\frac{\partial w}{\partial x}\right)^2 - w\frac{\partial^2 w}{\partial x^2}\right]\right.\\
&\qquad \left. + L_1(u,w) + L_2(w,w)\right\} + q - \frac{\partial^2 w}{\partial t^2} - \varepsilon_1 \frac{\partial w}{\partial t} = 0,\\
&L_1(u,w) = \frac{\partial^2 u}{\partial x^2}\frac{\partial w}{\partial x} + \frac{\partial u}{\partial x}\frac{\partial^2 w}{\partial x^2};\\
&L_2(w,w) = \frac{3}{2}\left(\frac{\partial w}{\partial x}\right)^2 \frac{\partial^2 w}{\partial x^2}; \quad L_3(w,w) = \frac{\partial w}{\partial x}\frac{\partial^2 w}{\partial x^2},
\end{aligned} \tag{19}$$

where: $L_1(u,w)$, $L_2(w,w)$, $L_3(w,w)$ are non-linear operators; $w(x,t)$, beam element normal deflection; $u(x,t)$, beam element longitudinal displacement; ε_1, damping factor; E, Young modulus; h, height of transversal beam cross section; γ, specific beam material density; g, Earth acceleration; k_x, beam geometric curvature; t, time; $q = q_0 \sin(\omega_p t)$, external excitation; q_0, amplitude of excitation; ω_p, excitation frequency. Non-dimensional quantities follow (bars over non-dimensional parameters are omitted in Eqs. (19))

$$\begin{aligned}
&\lambda = \frac{a}{h}; \quad \bar{w} = \frac{w}{h}; \quad \bar{u} = \frac{ua}{h^2}; \quad \bar{x} = \frac{x}{a}; \quad \bar{t} = \frac{t}{\tau};\\
&\tau = \frac{a}{p}; \quad p = \sqrt{\frac{Eg}{\gamma}}; \quad \bar{\varepsilon} = \frac{a}{p}; \quad \bar{q} = \frac{qa^4}{h^4 E}; \quad \bar{k}_x = \frac{k_x a}{\lambda}.
\end{aligned} \tag{20}$$

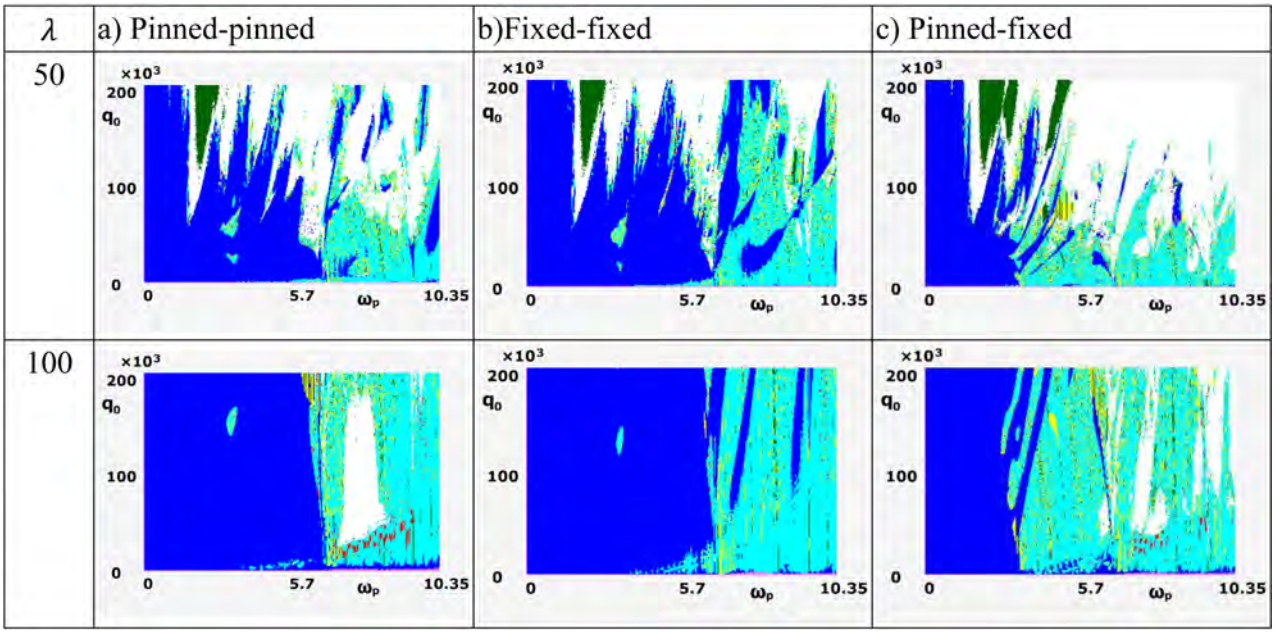

FIG. 21. Vibration charts versus λ and boundary conditions.

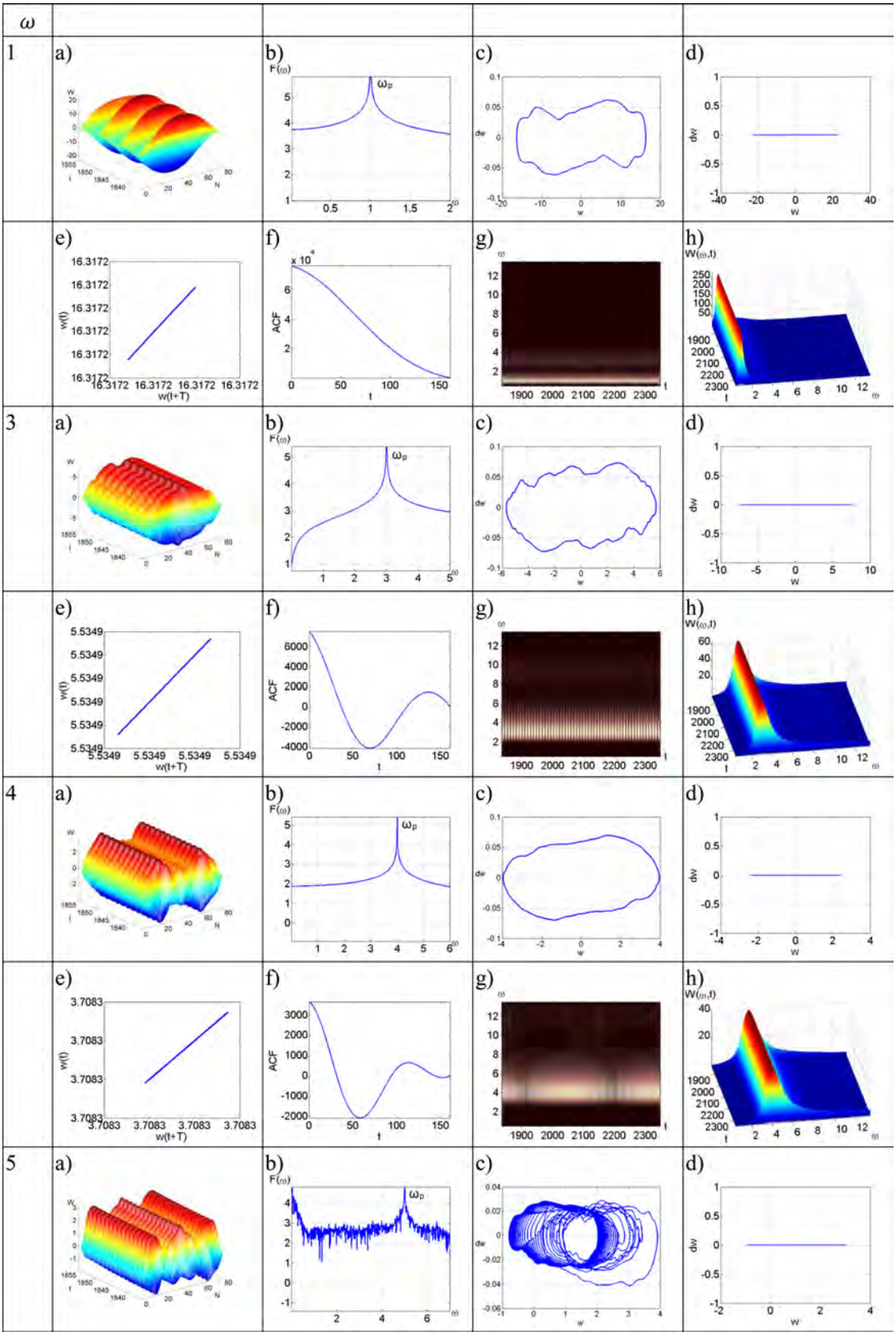

FIG. 22. Beam vibration characteristics.

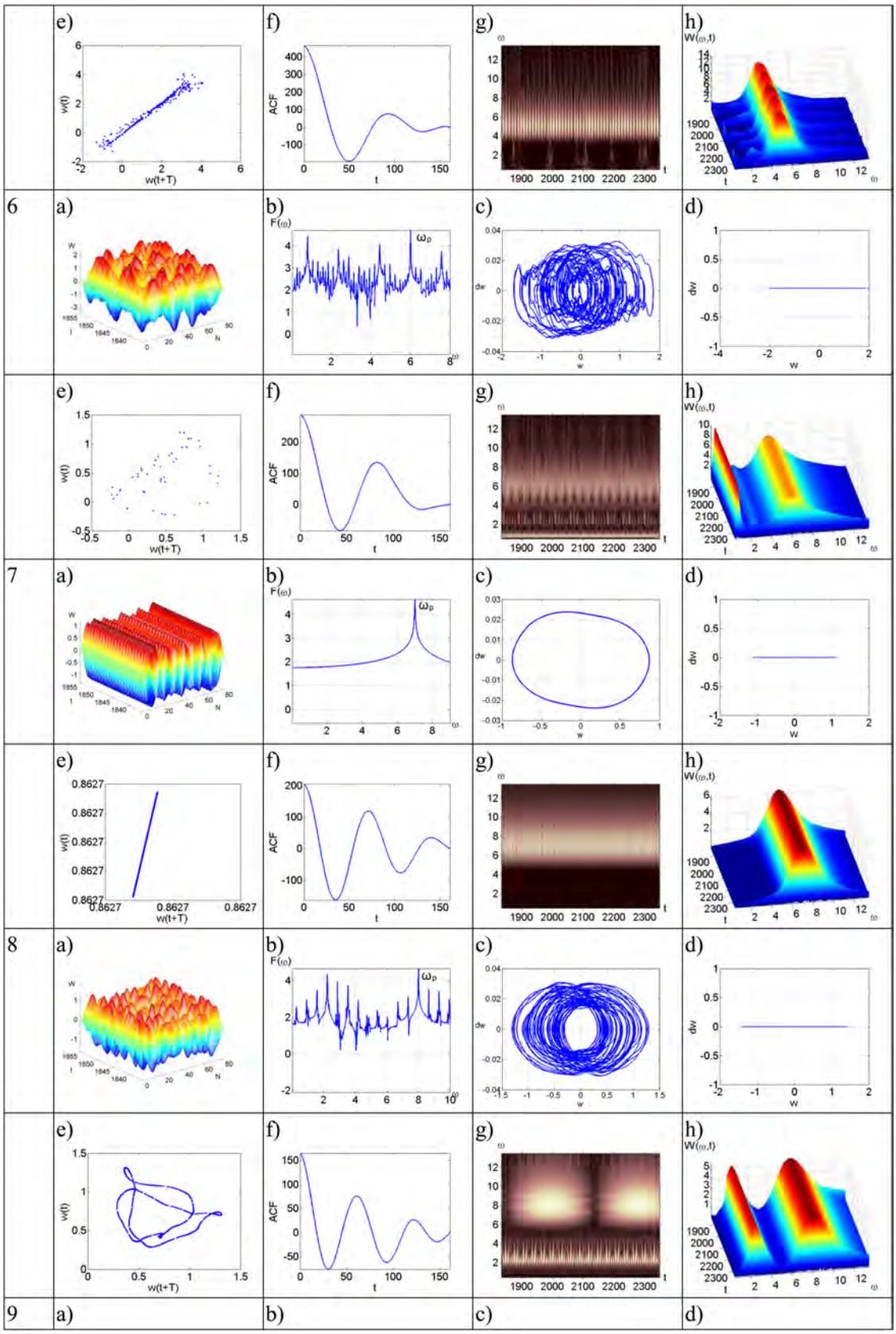

FIG. 22. (*Continued*)

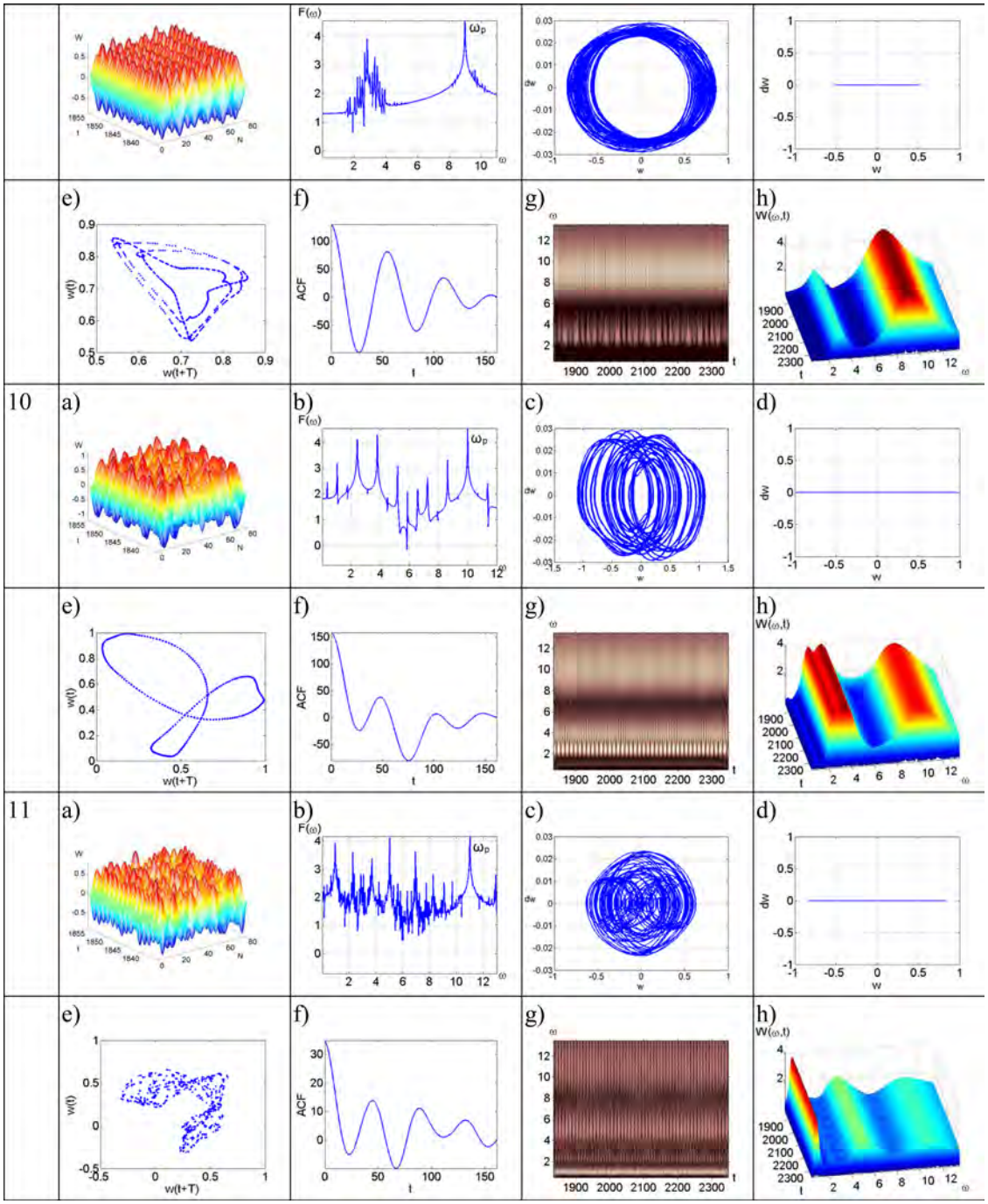

FIG. 22. (*Continued*)

One beam end is pinned ($x = 0$), whereas the second one is fixed ($x = a$)

$$w(0,t) = w(a,t) = u(0,t) = u(a,t) = w'_x(a,t) = w''_{xx}(0,t) = 0, \tag{21}$$

and the initial conditions have the form

$$w(x,0) = \dot{w}(x,0) = u(x,0) = \dot{u}(x,0) = 0. \tag{22}$$

B. Method of solution and numerical results

The system of PDEs (19)–(22) is reduced to ODEs via FDM of the second order and FEM, and then it is solved via both fourth and sixth-order? Runge-Kutta methods.

The following characteristics are constructed:

(1) Fourier power spectrum, Poincaré map, phase portrait—$w(\dot{w})$, modal portrait $(w(w'_x))$, autocorrelation function for x = 0.5, deflection graph for a given time instant, changes of beam deflections $w(x,t)$ in the given time instants, 2D and 3D Morlet wavelets. For $q_0 = 86\,500$ (Figure 23(a)), the Fourier spectrum exhibits only one excitation frequency $\omega_p = 5.7615$. Elliptic form of the phase curve implies beam periodic vibrations. Maximum beam deflection is shifted into left, since we have non-symmetric boundary conditions.

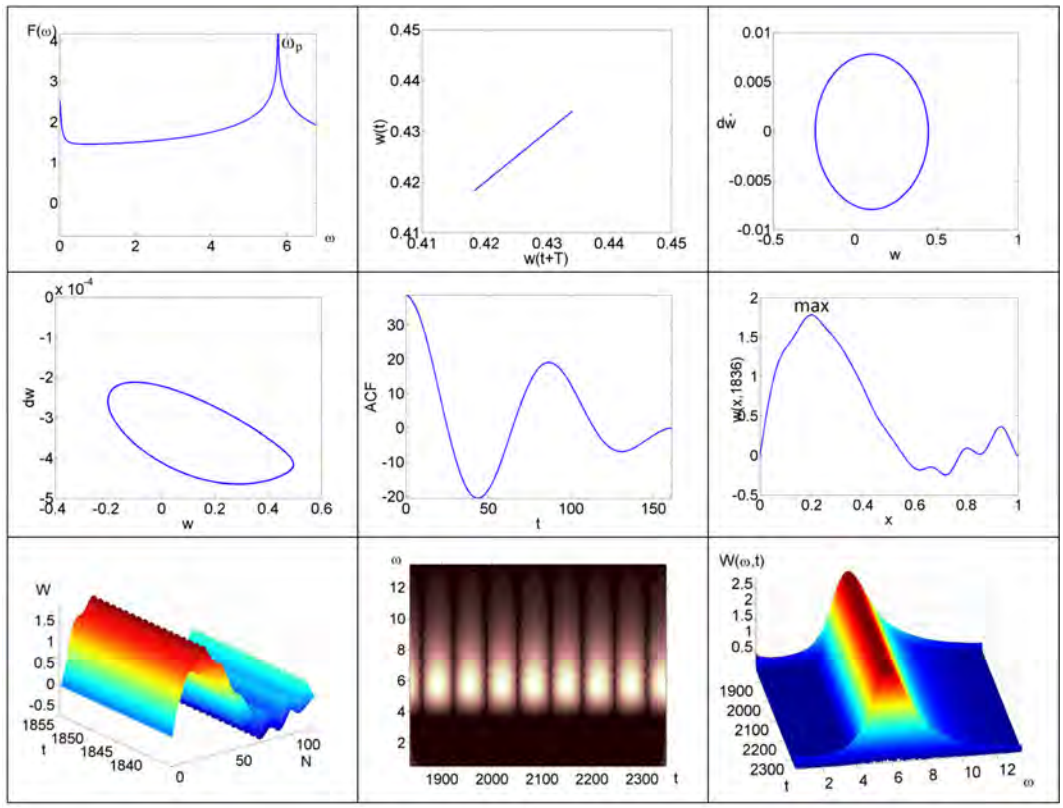

(a)

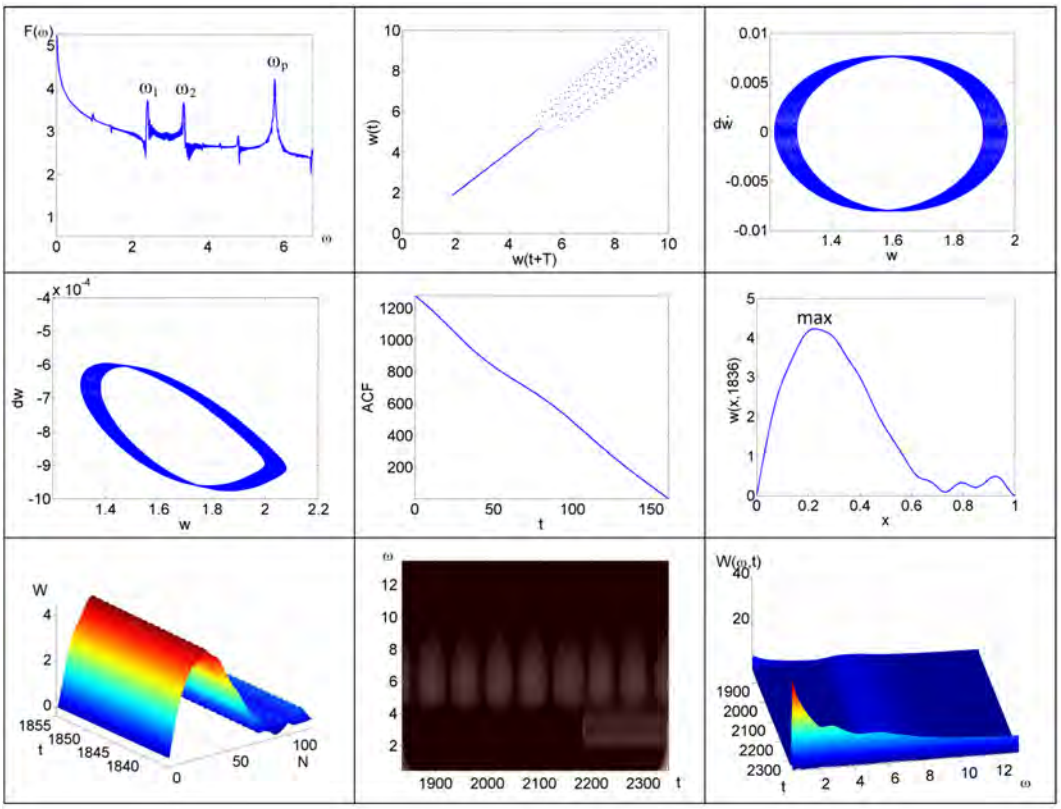

(b)

FIG. 23. (a) $q_0 = 86\ 500, \quad \omega_p = 5,76151$, (1) Fourier power spectra, (2) Poincaré pseudo-maps, (3) phase portraits, (4) modal portraits, (5) autocorrelation functions (ACF), (6) beam deflections for $t = 1836$, (7) 3D beam deflections in time interval $t \in [1836,\ 1852]$, (8) 2D Morlet wavelets, (9) 3D Morlet wavelets. (b) $q_0 = 87\,000, \quad \omega_p = 5,76151$. (c) $q_0 = 87\,500$, $\omega_p = 5,76151$; (d). $q_0 = 198\,000, \quad \omega_p = 5,7615$.

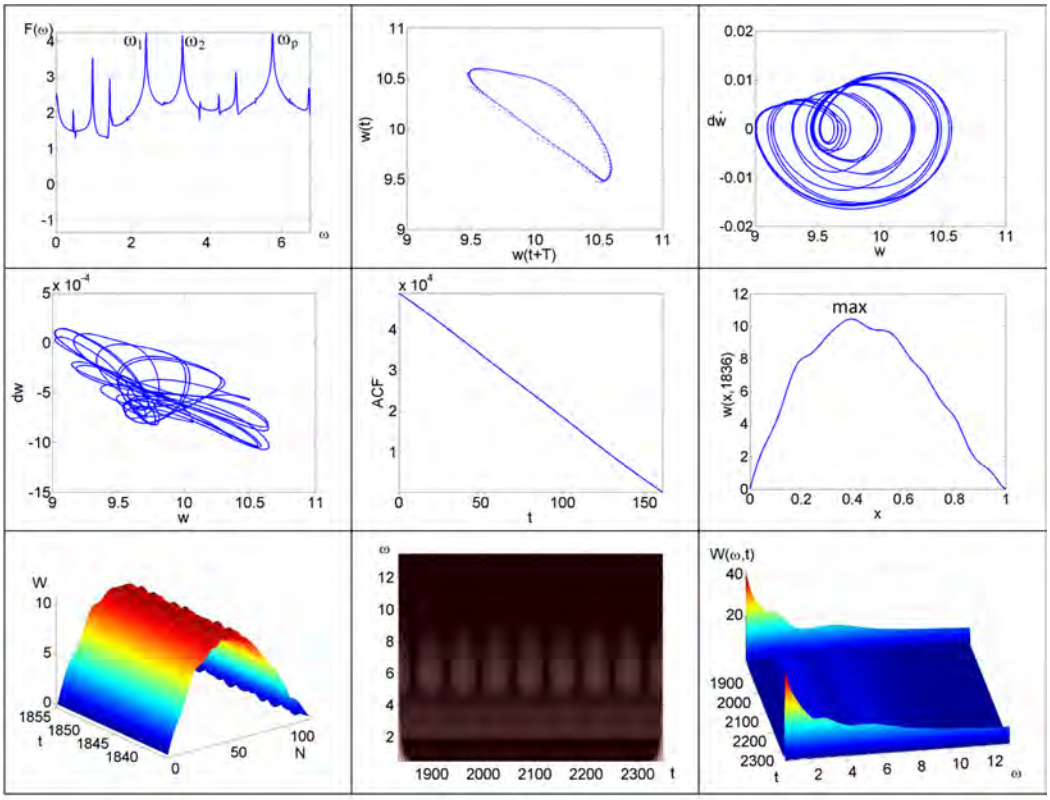

(c)

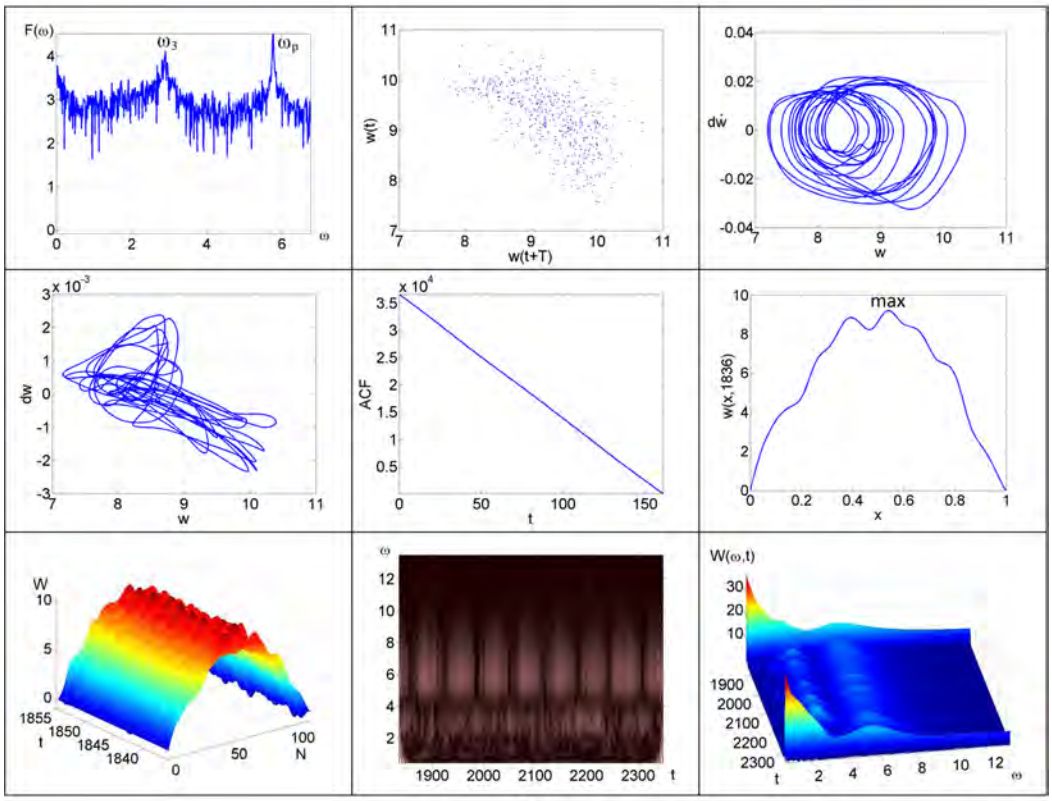

(d)

FIG. 23. (*Continued*)

(2) Increasing of the excitation amplitude up to $q_0 = 87\,000$ (Figure 23(b)) yields a new independent frequency, and a linear combination of this frequency and excitation frequency takes place. Phase portrait is thicker, the autocorrelation function decreases, the deflection graph is non-symmetric, and its maximum value achieves an order of four beam thicknesses. The wavelet spectrum exhibits only one excitation frequency for $t \in (0; 1180)$, and beginning with $t = 1180$ a new frequency birth is reported. Note that the linear combination of frequencies on the wavelet spectrum is not visible because their energy is essentially lesser than that of two exhibited frequencies.

(3) A further increase of our control parameter up to $q_0 = 87\,500$ (Figure 23(c)) implies the system stability loss, understood in the way that a slight load increase yields large deflection increase. Maximum deflection graph is shifted. New frequencies, produced via linear combination of the independent and excitation frequencies, appear in the power spectrum. The space signal presents the beam equilibrium position shift which corresponds to the dynamic stability loss. Wavelet spectrum displays three frequencies in the whole time interval. Phase portrait reports a belt type attractor which is also shown in the modal portrait. Poincaré portrait contains a closed curve.

(4) Increase of the loading amplitude up to $q_0 = 198\,000$ (Figure 23(d)) forces the system transition into a deeper chaotic state, which is indicated by a cloud-type points distribution of the Poincaré map. Power spectrum displays a key role of the frequencies ω_p and $\frac{\omega_p}{2}$ in the chaotic beam dynamics. Wavelet spectrum is of the broad band shape.

X. CONCLUDING REMARKS

The following main concluding remarks can be formulated:

1. We investigated numerically the chaotic dynamics of flexible Euler-Bernoulli beams.
2. The validity and reliability of the results obtained were guaranteed by the coincidence of solutions obtained using two different approaches. Namely, the reduction of PDEs into ODEs was carried out through FDM and FEM. The Cauchy problem was solved via the fourth and sixth-order? Runge-Kutta methods. Convergence of the solutions versus the beam partitions number was studied. The value of $n = 120$ allowed us to treat the system as the one with infinite degrees of freedom which was validated by the full coincidence of the Fourier power spectra, wavelet analysis, time histories, and other characteristics applied.
3. We described various transitions into chaotic and hyperchaotic vibration regimes of the investigated Euler-Bernoulli beams.
4. We also illustrated and discussed the temporal-space chaotic dynamics of the studied beam, which to our knowledge, has not been reported in the available literature and web sources. This has been achieved by analyzing the modal portraits (w, w'_x, w''_{xx}) that characterize the beam bending, rotation of the tangent for $\forall x \in [0, 1]$, and the approximating beam curvature. The applied modal portrait is analogous to the widely used phase portrait, and it exhibits the system evolution in time. It is remarkable that the scenario of transition of the studied system from regular dynamics into chaos was realized simultaneously in time and space.
5. Fixing the transversal load excitation amplitude and changing its frequency within the interval $\omega_p \in (0, 10.35]$ implies the mode change with regard to x beginning from 1 to 7 half-waves.
6. Vibration type charts were constructed in the plane $\{q_0; \omega_p\}$ for three types (3), (4), (5) of the boundary conditions which makes it possible to easily control the beam dynamics, and in particular to omit dangerous beam vibrations.
7. Spatio-temporal chaos exhibited by a curvilinear Euler-Bernoulli beam has been illustrated and discussed.

ACKNOWLEDGMENTS

The research was supported by the MAESTRO2 grant of the Polish National Foundation of Science (NCN) for the years 2013-2016. J. Awrejcewicz acknowledges a support of the Alexander von Humboldt Award.

[1]H.-C. Wang, ASME J. Appl. Mech. **34**, 702 (1967).
[2]J.-C. Hsu, H. Y. Lai, and C. K. Chen, J. Sound Vib. **325**, 451 (2009).
[3]W. Yeih, J. T. Chen, and C. M. Chang, Eng. Anal. Boundary Elem. **23**, 339 (1999).
[4]J. Moon and J. A. Wickert, J. Sound Vib. **200**(4), 419 (1997).
[5]M. Abu-Hilal, J. Sound Vib. **267**, 191 (2003).
[6]S. Gutschmidt and O. Gottlieb, J. Sound Vib. **329**, 3835 (2010).
[7]C. W. Lim, C. M. Wang, and S. Kitipornchai, Arch. Appl. Mech. **67**, 179 (1997).
[8]P. Shi, J. McPhee, and G. R. Heppler, Multibody Syst. Dyn. **5**(1), 79 (2001).
[9]H. Zohoor and S. M. Khorsandijou, J. Nonlinear Dyn. **51**(1–2), 217 (2007).
[10]E. Hall, S. Kessler, and S. Hanagud, Appl. Mech. Rev. **44**, 107 (1991).
[11]N. S. Abhyankar, E. K. Hall, and S. V. Hanagud, J. Appl. Mech. **60**(1), 167 (1993).
[12]P. Z. Bar-Yoseph, D. Fisher, and O. Gottlieb, Comput. Mech. **19**(1), 136 (1996).
[13]Ü. Lepik, Est. J. Eng. **17**(3), 271 (2011).
[14]J. Awrejcewicz, A. V. Krysko, M. V. Zhigalov, O. A. Saltykova, and V. A. Krysko, Lat. Am. J. Solids Struct. **5**(4), 319 (2008).
[15]J. Awrejcewicz, A. V. Krysko, J. Mrozowski, O. A. Saltykova, and M. V. Zhigalov, Acta Mech. Sin. **27**(1), 36 (2011).
[16]J. Awrejcewicz and A. V. Krysko, Arch. Appl. Mech. **73**, 495 (2003).
[17]J. Awrejcewicz, V. A. Krysko, and A. V. Krysko, Meccanica **39**(3), 221 (2004).
[18]V. A. Krysko, J. Awrejcewicz, and T. V. Shchekaturova, Arch. Appl. Mech. **74**(5–6), 338 (2005).
[19]J. Awrejcewicz, V. A. Krysko, and T. V. Shchekaturova, Int. J. Struct. Stab. Dyn. **5**(3), 359 (2005).
[20]V. A. Krysko, J. Awrejcewicz, N. E. Saveleva, and A. V. Krysko, Differ. Equ. Nonlinear Mech. **2006**, 59709 (2006).
[21]J. Awrejcewicz, V. A. Krysko, and V. Nazar'iantz, Commun. Nonlinear Sci. Numer. Simul. **12**(4), 519 (2007).
[22]A. V. Krysko, J. Awrejcewicz, E. S. Kuznetsova, and V. A. Krysko, Shock Vib. **15**(3–4), 223 (2008).
[23]J. Awrejcewicz, A. V. Krysko, and V. Soldatov, Int. J. Bif. Chaos **19**(10), 3347 (2009).

[24]P. S. Landa and P. V. E. McClintock, J. Phys. A: Math. Theor. **44**, 475501 (2011).
[25]C. Touzé, O. Thomas, and M. Amabili, Int. J. Non-Linear Mech. **46**(1), 234 (2011).
[26]K. Nagai, S. Maruyama, T. Murata, and T. Yamaguchi, J. Sound Vib. **305**(3), 492 (2007).
[27]S. Maruyama, K. Nagai, and Y. Tsuruta, J. Sound Vib. **315**(3), 607 (2008).
[28]G. Düring, Ch. Josserand, and S. Rica, Phys. Rev. Lett. **97**, 025503 (2006).
[29]A. Boudaoud, O. Cadot, B. Odille, and C. Touzé, Phys. Rev. Lett. **100**, 234504 (2008).
[30]O. Cadot, A. Boudaoud, and C. Touzé, Eur. Phys. J. B **66**(3), 399 (2008).
[31]N. Mordant, Phys. Rev. Lett. **100**, 234505 (2008).
[32]B. Miquel and N. Mordant, Phys. Rev. E **84**, 066607 (2011).
[33]N. Yokoyama and M. Takaoka, Phys. Rev. Lett. **110**, 105501 (2013).
[34]P. Cobelli, P. Petitjeans, A. Maurel, V. Pagneux, and N. Mordant, Phys. Rev. Lett. **103**, 204301 (2009).
[35]J. Awrejcewicz, O. A. Saltykova, M. V. Zhigalov, P. Hagedorn, and V. A. Krysko, Int. J. Aerosp. Lightweight Struct. **1**(2), 203 (2011).
[36]J. Awrejcewicz, A. V. Krysko, V. Soldatov, and V. A. Krysko, J. Comput. Nonlinear Dyn. **7**(1), 011005-1 (2012).
[37]J. Awrejcewicz, I. V. Papkova, E. U. Krylova, and V. A. Krysko, Shock Vib. **19**, 979 (2012).
[38]J. Awrejcewicz, A. Krysko, I. Kutepov, N. Zagniboroda, M. Zhigalov, and V. Krysko, Int. J. Struct. Stab. Dyn. **13**(7), 1340005-1 (2013).
[39]V. A. Krysko, J. Awrejcewicz, I. E. Kutepov, N. A. Zagniboroda, I. V. Papkova, A. V. Serebryakov, and A. V. Krysko, Phys. Lett. A **377**, 2058–2061 (2013).
[40]A. Grossmann and J. Morlet, SIAM J. Math. Anal. **15**(4), 723 (1984).
[41]G. Benettin, L. Galgani, A. Giorgilli, and J.-M. Strelcyn, Meccanica **15**(1), 9 (1980).
[42]K.-U. Schaumlöffel, Lect. Notes Math. **1486**, 187 (1991).
[43]H.-L. Yang, K. A. Takeuchi, F. Ginelli, H. Chaté, and G. Radons, Phys. Rev. Lett. **102**, 074102-1 (2009).
[44]A. Wolf, J. B. Swift, H. L. Swinney, and J. A. Vastano, Physica D **16**(3), 285 (1985).
[45]I. S. Arson and L. Kramer, Rev. Mod. Phys. **74**, 99 (2002).
[46]N. Bekki and K. Nozaki, Phys. Lett. A **110**(3), 133 (1985).
[47]H. Chaté, Nonlinearity **7**, 185 (1994).
[48]H. Chaté and P. Manneville, Physica A **224**, 348 (1996).
[49]T. Hogg and B. A. Huberman, Phys. Rev. A **29**(8), 275 (1984).
[50]R. Van Buskirk and C. Jeffries, Phy. Rev. A **31**(5), 3332 (1985).
[51]V. S. Afraimovich and V. I. Nekorkin, Int. J. Bifurcation Chaos **4**(3), 631 (1994).
[52]N. Koppel, G. B. Ermentrout, and T. L. Williams, SIAM J. Appl. Math. **51**(5), 1397 (1991).
[53]N. Kopell, W. Zhang, and G. B. Ermentrout, SIAM J. Math. Anal. **21**(4), 935 (1990).
[54]G. B. Ermentrout and N. Kopell, SIAM J. Appl. Math. **54**(2), 478 (1994).
[55]K. A. Sigvardt and T. L. Williams, Semin. Neurosci. **4**(1), 37 (1992).